Noise Spikes of Relaxation Oscillator from Energy Theoretic Approach

by

Yon Chiet Ng

A thesis
presented to the University of Waterloo
in fulfillment of the
thesis requirement for the degree of
Master of Applied Science
in
Electrical and Computer Engineering

Waterloo, Ontario, Canada, 2017

I hereby declare that I am the sole author of this thesis. This is a true copy of the thesis, including any required final revisions, as accepted by my examiners.

I understand that my thesis may be made electronically available to the public.

Abstract

An energy theoretic approach to augment the existing noise model is proposed by including the cryogenic (down to 77K) behaviour of the noise spikes due to the regeneration process (when loop gain $\rightarrow$ 1) of a relaxation oscillator. This noise model is useful in many time domain applications, e.g., design of $\Sigma\Delta$ Time-to-Digital Converter (TDC) at cryogenic temperature for quantum computing [1] with relaxation oscillator. The loop gain can be lowered towards 1 to increase the oversampling frequency, and subsequently reduce the quantization noise. The presented noise model tackles the noise spike problem from regeneration when $g_m R \rightarrow 1$.

Three methods are used to obtain the noise model. The first method, a first attempt, is to identify the potential energy of the macroscopic behaviour of the Schmitt trigger (an integrated component of relaxation oscillators) with the underlying assumption that the system can be represented by one degree of freedom. Investigation on the dynamics of the Schmitt trigger shows a metastable state (maximum energy) and two stable states (minimum energy) which is due to the cross-coupled topology of the circuit. The limitation of this method is that it ignores the internal degrees of freedom i.e the thermodynamic aspects appearing as temperature varies (decreases to cryogenic temperature). This limitation is then addressed in the second method by accounting for the different configurations in which these internal degrees of freedom manifest, resulting in the distribution of energy among the different configurations. The concept of free energy is introduced and from the free energy, the noise model obtained is now in function of temperature. As temperature drops further, quantum aspects start to arise. A third method is introduced as the temperature of the oscillator decreases and addresses the manifestation of quantum mechanical effect (at low temperature limit) with the assumption that the system is represented by one degree of freedom (macroscopic behavior), but with internal degrees of freedom represented by the immersion of the system in a heat bath with many degrees of freedom. The model for this method agrees with the second method when $g_m R \rightarrow 1$ at high temperature limit, thus giving us the confidence for the counterpart noise model at low temperature limit, where the quantum mechanical effects show up.

The experimental results of relaxation oscillators, designed and fabricated in 130nm CMOS technology, show two regions with different slopes: at higher temperature, the phase noise is consistent with the noise model prediction where the phase noise (from thermal noise) is proportional to $\sqrt{T}$; at lower temperature, the phase noise becomes relatively constant and the trend agrees rather well with noise model (quantum noise) at low temperature limit. By changing the regeneration time of the relaxation oscillator (doubling $\frac{W}{L}$ of transistors), there is a shift of the crossover temperature of the two regions,

which is as predicted by the noise model. Finally, a 1-bit $\Sigma\Delta$ TDC is designed, and fabricated, using the relaxation oscillator, and the measured functional operation of the TDC agrees with simulations.

Acknowledgements

I would like to express my gratitude to my supervisors, Professor Bosco Leung and Professor Safieddin Safavi-Naeini, for their guidance, support and encouragements. I would like to thank Professor Hamed Majedi for his generosity by allowing me to use his lab for cryogenic experiments, and his students, Milad Khoshnegar Shahrestani, Jing Xu and Sid Thakur for helping me to set up the experiment and giving me the access to the lab even during the weekends.

I would like to thank Peter Schweiger from Keysight for his kind gesture of loaning the Spectrum Analyzer for the experiment, Gholamreza (Reza) Z. Rafi for allowing me to use the equipment from their lab and CMC Microsystem for their excellent service and continuous support for equipment loan. I would like to also give my warm thanks to Albert Wasef and Manisha Shah for their kindness of letting me to do some oscilloscope measurements in the undergraduate lab. Also, many thanks to Phil Regier for his support in computer-related problems.

I would like to thank Luxsumi Jeevananthan for her advice in the chip layout and Jianian Tao for his help in the past few years. Last but not the least, I would like to thank all my friends and my family for their love and their continuous support.

Table of Contents

List of Tables

List of Figures

Chapter 1

Introduction

The relaxation oscillator is widely used as a low-power on-chip reference clock generator in biomedical applications [3] [4], including body area network receivers [5], and time-to-digital converter [6]. The rising interest in portable devices demands low power and low cost circuit implementations. For health monitoring applications such as pacemaker, an intermittent power system [7] that operates between active mode and sleep mode could reduce the power consumption significantly. The wake-up function of such system is inevitable and can be implemented by using oscillators such as crystal oscillators, LC oscillators, ring oscillators and relaxation oscillators. Crystal oscillators are bulky and cannot be implemented for on-chip system. LC oscillators demand large area on chip because of the large on-chip inductor. Ring oscillators can have noise arising from cycle to cycle correlation from across delay cell stages. Since relaxation oscillators have low power consumption and have small size, they are favored for such applications. However, with regeneration, relaxation oscillators are more susceptible to noise spikes. The focus of this thesis is to present a phase noise model for the source (emitter)-coupled pair relaxation oscillator. The past works of phase noise model on oscillators include the first order analysis of linear oscillatory system [8] and threshold crossing [9]. However, these noise models do not apply to oscillator with noise spikes, which becomes more prominent as the loop gain $g_m R$ (governing regeneration) of the positive feedback loop is lowered towards 1, thus limiting the frequency of the oscillator [10]. For relaxation oscillators in applications such as $\Sigma\Delta$ TDC, this limits the oversampling frequency, and subsequently increases the quantization noise. On the other hand, a relaxation oscillator with $g_m R \to 1$ suffers from the noise spike problem [11] [12] caused by the positive feedback of the regeneration process. The presented noise model, like [11], tackles the noise spike problem. Yet, instead of using a nonlinear dynamic approach, an energy theoretic approach [13] is applied. This more physics

oriented approach extends the predictive power of the model to wide range of operating temperature and has potential applicability to TDC design for quantum computing [1].

A relaxation oscillator can be constructed with Schmitt trigger and timing components (R, C) [14]. The dynamics of the relaxation process consists of the fast time scale, which is governed by the dynamic of the Schmitt trigger, and the slow time scale, which is governed by the charging/discharging of the capacitor. Since the noise spikes occurs during the fast dynamic of the system, i.e., the regenerative process of the Schmitt trigger, the current fluctuation of the Schmitt trigger during metastability is crucial in determining the fluctuation of the relaxation oscillator. A first attempt on analyzing this metastability is given in [11]. [11] interprets the potential from the point of view of the gradient of vector field, which is more of a nonlinear dynamic system approach [12]. In this work, a noise model of the relaxation oscillator is obtained with energy theoretic approach

This thesis is constructed as following: in Chapter 2, the potential of the gradient of vector field is now rederived using physics from first principles. This is first by identifying the potential energy of the macroscopic behavior of the system with the underlying assumption that the system can be represented with one degree of freedom (the coordinate of the whole system; in this case, the coordinate is the current). The limitation of this method is that it ignores the internal degree of freedom, or namely, the ensemble's individual coordinates (the charges distribution over energy levels in phase space/eigenenergies).

This limitation is further addressed in Chapter 3 by accounting for the different configurations in which these internal degrees of freedom manifest, resulting in the distribution of energy among the different configurations, and thus energy becomes free energy(with the entropy in the free energy reflecting the different configurations). The fluctuation is then carried out by standard thermodynamic procedure from free energy. From the free energy, the noise model for the Schmitt trigger can be ontained and it is consistent to the noise model presented in [11].

As temperature decreases, the manifestation of quantum mechanical effect is taken into account. Calculation of energy levels in phase space becomes calculation of eigenenergies, which is difficult. Meanwhile, the free energy gives the complete thermodynamic information (e.g. heat capacity) of the system, of which only the fluctuation is of our interest. Noting the above, and for simplification, in Chapter 4, the system is represented by one degree of freedom (macroscopic behavior), but the internal degree of freedom is 'decoupled' and is represented by the 'immersion' of the system in a a heat bath with many degree of freedom, manifesting in the dissipation (microscopic) of the system. This can be done by essentially a Langevin approach, which incorporates quantum effect in the heat bath with many degree of freedom. Meanwhile, the classical fluctuation solution of the Langevin

approach [15] yields a solution that agrees with the full blown free energy approach, justifying this Langevin approach. The result shows consistency with the noise model provided by [11] and obtained in Chapter 2 at high temperature limit regime. In addition, it also provides perspective into low temperature limit regime of the relaxation oscillator. The above is summarized in table 1.1 in Chapter 1.2.

The relaxation oscillators are designed with 130nm CMOS technology. In Section 5, the experimental phase noise data of the relaxation oscillators are presented. The experimental results show two regions with different temperature trend: at higher temperature, the phase noise is proportional to $\sqrt{T}$ as predicted by the noise model. At lower temperature, the phase noise becomes relatively constant and is consistent with quantum mechanical model.

This noise spike model is applicable in the application of relaxation oscillator in TDC. By having $g_m R \to 1$, the oscillator noise spikes up but the oscillator frequency also increases, resulting in oversampled frequency of $\Sigma\Delta$ TDC [6], using such a relaxation oscillator, increases, hence the oversampling ratio increases. Hence, the quantization noise is lowered. In Section 6, the functional operation of the TDC is discussed.

1.1 Types of Relaxation Oscillators

A relaxation oscillator is an astable circuit with regenerative switching. It switches continuously between the two unstable states by charging and discharging the timing capacitor. The frequency of the output waveform is proportional to the value of the timing capacitor. Because of its regenerative switching, it produces fast changing output in response to slow-changing input, which gives a square-wave output waveform. Depending on the configurations of the relaxation oscillator, it can be classified in three groups:

1. RC relaxation oscillator that use resistive charge and discharge path for the timing capacitor

2. Constant-current relaxation oscillator that use current sources to charge and discharge the timing capacitor

3. Emitter-coupled/source-coupled multivibrators with timing capacitor across the emitter/source of the differential gain stage

1.1.1 RC Relaxation Oscillator

A conventional RC relaxation oscillator is shown in Figure 1.1. Typically, it consist of three main functions:

1. It has timing components R, C. R_1 is responsible for the charging of C_1 and R_2 is responsible for the discharging of C_1.
2. It consists of a Schmitt trigger (i.e. a comparator with hysteresis).
3. It has a grounding switch, S_1, which is part of the feedback from the output. The switch is usually implemented using a MOS or BJT transistor.

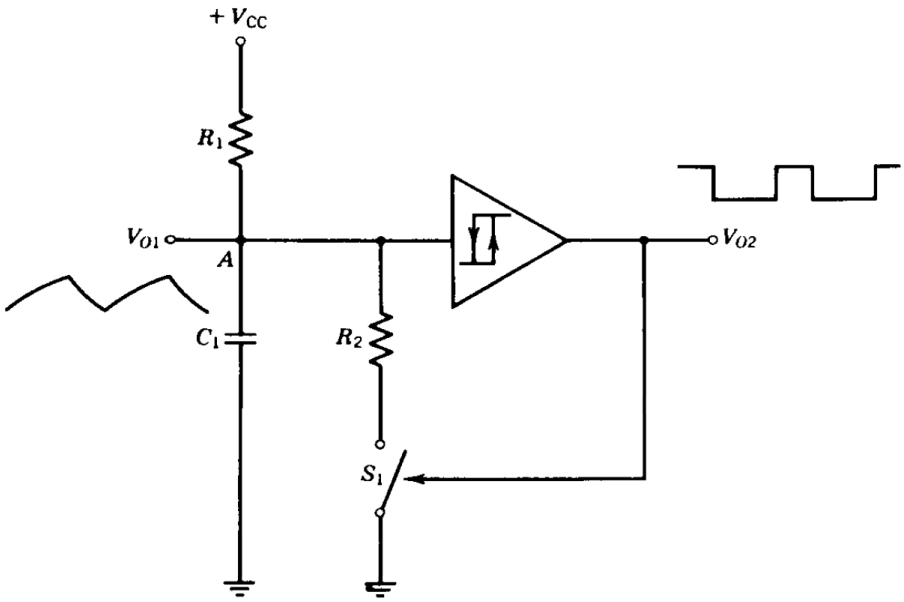

Figure 1.1: RC Relaxation Oscillator [2]

Schmitt trigger is a regenerative circuit with upper switching threshold, V_B and lower switching threshold, V_A. When the input voltage of Schmitt trigger, $V_{o1} > V_B$, it triggers the regenerative process and the output is switched to the positive state, L_+. On the other hand, when $V_{o1} < V_A$, the output settles to the negative state, L_-.

The operation of an RC relaxation oscillator works as following: Initially, the switch, S_1 is open and C_1 is charging through the resistor, R_1. V_{o1} is increasing and when it crosses

the upper switching threshold, V_B of the Schmitt trigger, regeneration is triggered and the output switches to the positive state, L_+. This, in turn, closes the switch, S_1, which provides a discharging path for the capacitor. V_{o1} decreases and crosses the lower switching threshold, V_A. This prompts the output to switch immediately to the negative state, L_-. The switch, S_1 is open. The operation repeats itself and the output switches between the positive state, L_+ and the negative state, L_- continuously.

Schmitt trigger is critical to the operation of the relaxation oscillator. This is because the frequency of the relaxation oscillator depends on the stability and accuracy of the upper/lower threshold voltage of the Schmitt trigger. A commonly used Schmitt trigger for high-performance relaxation oscillator is the dual-comparator type Schmitt trigger. This circuit consists of the biasing resistors, comparators and SR flip-flop.

1.1.2 Constant-Current Relaxation Oscillator

A constant-current relaxation oscillator as shown in Figure 1.2 consists of timing capacitor, C_1, the current source, I_1, I_2, and Schmitt trigger. The operation of the relaxation oscillator is similar to an R-C relaxation oscillator, but instead of using resistors for charging and discharging the capacitor, current sources are used.

The current source, I_1 is always on while the current source, I_2 is off. When the output of the relaxation oscillator is at the negative state, L_-, the timing capacitor, C_1 is charged and V_{O1} increases with slope $\frac{I_1}{C_1}$. When the output of the relaxation oscillator is at the positive state, L_+, C_1 is discharged since I_2 is designed to be larger than I_1. Thus, V_{O1} decreases with slope $\frac{I_2-I_1}{C_1}$.

1.1.3 Emitter/Source-coupled multivibrator

An emitter/source-coupled multivibrator has symmetrical charge and discharge paths for the timing capacitor, C. An example of a source-coupled multivibrator is shown as Figure 1.3. The circuit comprises of two matching resistors, two transistors, M_1 and M_2 which are biased with the matched current sources and is coupled through timing capacitor, C. For symmetrical operation, M_1 and M_2 have matched design parameters.

The operation of the source-coupled relaxation oscillator is as follows. At metastable state, M_1 and M_2 are in saturation, and the voltage across the capacitor, $V_C = 0$. When $V_C > 0$, the current flowing through M_1 is less than the current flowing through M_2. This, in turn, causes the drain voltage of M_2 to decrease while the drain voltage of M_1 increases.

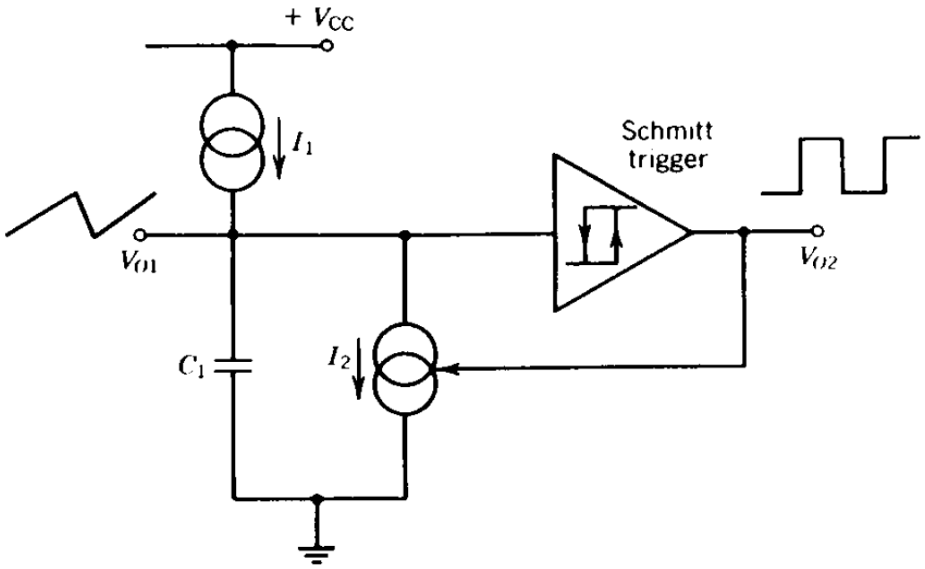

Figure 1.2: Constant-Current Relaxation Oscillator [2]

The voltage across the capacitor, V_C is charged up. When the gate-to-source voltage of M_1 is less than the threshold voltage, V_t, i.e. $V_{gs1} < V_t$, M_1 is off and the differential output $(V_{d1} - V_{d2})$ is at the positive state, L_+. The voltage across the capacitor, V_C will discharge to a point where M_1 conducts and M_2 turns off. Then, the differential output is at the negative state, L_-. The operation repeats and the circuit changes state continuously.

1.2 Review on the Previous Noise Models of Relaxation Oscillator

The noise problem tackled for the various noise models are summarized in Table 1.1. The noise spike does not manifest in [9], [16], [8] since the $g_m R$ of the relaxation oscillator is designed to be larger, but not close to 1. Hence, the noise models are incomplete for condition with design parameter $g_m R \to 1$, which is the main interest of this thesis. [12] includes the noise spike in the calculation, but identifies a singularity condition when the $\epsilon \to 0$, where the ϵ accounts as gross simplification of the parasitic capacitors in the circuit. [11] attempts to explain the jump phenomenon as the phase change of the thermodynamic systems such as Van de Waal (vdw) gas and Ising model. The nonlinear dynamic of the

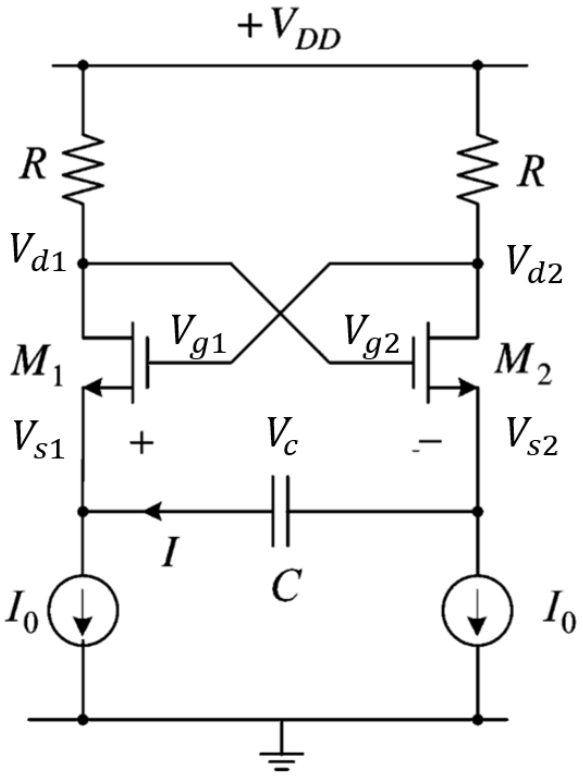

Figure 1.3: Circuit Diagram of Source-coupled Relaxation Oscillator

circuit is performed, with the energy from the gradient of vector field mapped to the free energy of the thermodynamic systems. Following [11], three methods are presented in this thesis. *Method 1* identifies the potential energy (with one metastable state and two stable states) of a Schmitt trigger a product of the symmetrical cross-coupled topology of the circuit. This relates the potential energy of the circuit with the circuit design parameters. It is shown that the metastable state gives maximum potential energy and the two stable states give minimum potential energy. *Method 2* is proposed by accounting the internal degree of freedom of the system, and thus gives the temperature dependency in the noise model. *Method 3* accounts for the possible manifestation of quantum noise effect when the temperature is lowered. The Langevin equation is simplified for a small region around the metastable state, where the fluctuation is maximized.

A brief background of [11]'s work is presented here. Given the circuit in Figure 1.3, the noise spikes, as shown in Figure 1.4, occur at the time of switching during the regeneration

Noise problems to be tackled	Works
Noise models with the absence of noise spikes caused by the regeneration properties of relaxation oscillator	[9], [16] , [8]
Noise model with noise spikes singularity observed	[12]
Noise model at room temperature with noise spikes included	[11] (*Method 1*): the nonlinear dynamics of relaxation oscillator is investigated, with energy from the gradient of vector field mapped to the free energy of thermodynamic systems. In chapter 2, the potential energy is identified using energetic theoretic approach
Noise model with noise spikes present(cryogenic behavior I)	Chapter 3 in this work (*Method 2*):Instead of mapping, the free energy of relaxation oscillator is directly calculated. Noise model is derived from the free energy.
Noise model with noise spikes present(cryogenic behavior II)	Chapter 4 in this work (*Method 3*): Noise model is derived from the Langevin equation of relaxation oscillator

Table 1.1: A comparison of the noise problems to be solved by the noise models among different works

process. This noise spike phenomenon is compared by [11] with the phase changes of thermodynamic systems such as Van der Waal gas (the transition from liquid to gas) or Ising model (magnetization of ferromagnet). Noting the mathematical resemblance between the pressure-volume trajectory of the vdw gas and the voltage-current trajectory of the relaxation oscillator, the fluctuation model of the vdw gas is mapped to the fluctuation model of the relaxation oscillator.

The trajectory of the vdw gas can be represented by the differential equations:

$$\frac{dp}{d\tau} = v \tag{1.1}$$

$$\epsilon_g \frac{dv}{d\tau} = 4\tau - p - 6\tau v - \frac{3}{2}v^3 \tag{1.2}$$

where ϵ_g is from the fast dynamics of the gas [12] ,p is the reduced pressure and v is the reduced volume of the vdw gas, τ is the reduced temperature. These variables are defined

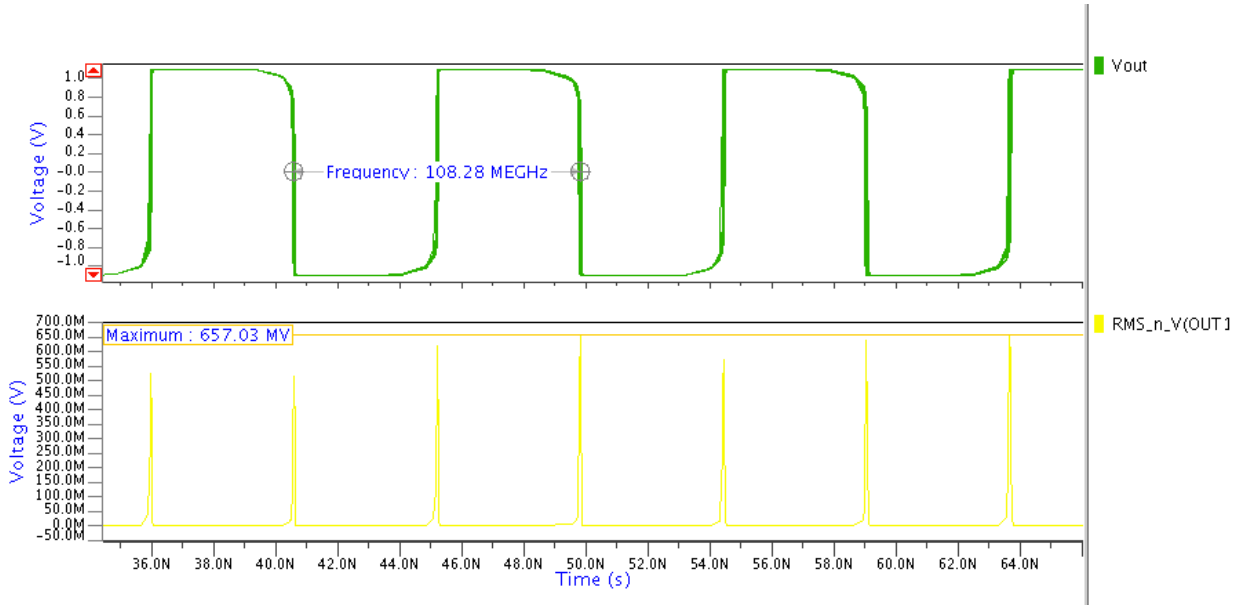

Figure 1.4: Noise spikes occurs at the metastable state of the relaxation oscillator. The simulation code is presented in Appendix A.1

as:

$$\begin{aligned} p &:= \frac{P - P_c}{P_c} \\ v &:= \frac{V - V_c}{V_c} \\ \tau &:= \frac{T - T_c}{T_c}, \end{aligned}$$

where P_c is critical pressure, V_c is critical volume, and T_c is critical temperature of the vdw gas. The density fluctuation of the vdw gas is calculated using Gibbs-Duhem equation [11] to be:

$$\frac{\langle (\delta\rho)^2 \rangle^{\frac{1}{2}}}{\rho} \propto \frac{1}{\sqrt{\frac{kT_c}{kT} - 1}}, \tag{1.3}$$

where ρ is the density of the gas and $\langle (\delta\rho)^2 \rangle$ is the variance of the density of the gas. It is shown in eq.(1.3) that when the temperature, T is near to the critical temperature, T_C, the

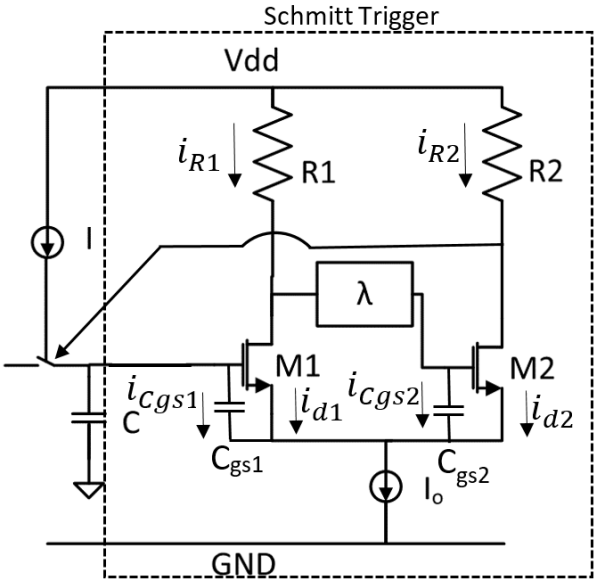

Figure 1.5: Ground Capacitor Relaxation Oscillator Model

density fluctuation spikes up. This phenomenon is compared to the output noise spikes of relaxation oscillator during the switching.

For the ground-capacitor relaxation oscillator topology as shown in Figure 1.5, the voltage-current trajectory can be described as below:

$$\frac{dV}{dt} = \frac{I}{C} \tag{1.4}$$

$$\epsilon\frac{di}{dt} = -\frac{g_m V}{I_0} + \sqrt{2}(1 - g_m R)i + \frac{1}{8}i^3. \tag{1.5}$$

V is the voltage across the capacitor, C. ϵ comes from the parasitic effect of the transistors, such that $\epsilon = \frac{RC_{gs}}{g_m}$ and i is the normalized current, $\frac{i_{d1}-i_{d2}}{I_0}$ The volume, v characterizes the fluctuation of the vdw gas. In the context of relaxation oscillator, the current, i is used to characterized the fluctuation. The differential equations of vdw gas, eq.(1.1), (1.2) is then mapped to the differential equations of the relaxation oscillator, eq.(1.4), (1.5). The mapping of variables between vdw gas and relaxation oscillator can be summarized

as shown:

$$\begin{aligned} p(pressure) &\leftrightarrow V(voltage) \\ v(volume) &\leftrightarrow i(current) \\ \tau(temperature) &\leftrightarrow t(time). \end{aligned}$$

To map the current fluctuation of relaxation oscillator to the density fluctuation of the vdw gas, the noise contribution of the relaxation oscillator is identified. The power spectral density of current thermal noise (contributed by the resistors) is given as

$$psd\ of\ 'i' = \frac{4kT}{R} + \frac{4kT}{R} \tag{1.6}$$

where k is the Boltzmann constant and T is the absolute temperature of the resistor. Eq (1.6) is calculated for one sided BW. To map it to the vdw gas, a two sided BW of eq (1.6) is used by dividing it by two. Then the mapping of the thermal noise contribution is shown as below:

$$kT \leftrightarrow \frac{4kT}{R}.$$

Then, the interaction mechanism of both vdw gas and relaxation oscillator is compared. The part that is responsible for the interaction energy of vdw gas is kT_C in eq (1.3). To map it to the relaxation oscillator, the interaction energy of the charges particle is found to be $qg_m^2RV_{peak}$ where V_{peak} is the voltage change in V, the voltage across capacitor. The mapping of the interaction energy between the vdw gas and relaxation oscillator is shown as

$$kT_c \leftrightarrow qg_m^2RV_{peak}.$$

By identifying the corresponding mapping between vdw gas and relaxation oscillator, eq (1.3) can be mapped to relaxation oscillator with current fluctuation

$$\frac{\left\langle \frac{(\delta i)^2}{\Delta f} \right\rangle^{\frac{1}{2}}}{i} \propto \frac{1}{\sqrt{\frac{eV_{peak}}{4kT}(Rg_m)^2 - 1}}. \tag{1.7}$$

1.3 Review of Previous Model on Potential Energy of Schmitt Trigger (In Ground Capacitor Based Relaxation Oscillator)

Figure 1.5 shows the application of a Schmitt trigger in the design of a relaxation oscillator [11]. The Schmitt trigger governs the regeneration process in the switching of states for a relaxation oscillator. For simplification, $R_1 = R_2 = R$, $k_{n1} = k_{n2} = k_n$. Previously, [11] ignores C_{gs2} and encapsulates the parasitic effects of C_{gs1} as $\epsilon = \frac{RC_{gs1}}{g_m}$ in (1.8). During the regeneration process Schmitt trigger is approximated by a first order differential equation in normalized current, $\Delta := \frac{2i_{d1}-I_0}{I_0}$ [1] as shown in (1.8):

$$\frac{d\Delta}{dt} = \frac{\sqrt{2}}{\epsilon}\left((1-g_mR)\Delta + \frac{1}{8}\Delta^3\right). \tag{1.8}$$

Then, [11] assumes (1.8) describes a first order system with a potential function [17], such that

$$\frac{d\Delta}{dt} = \frac{dE}{d\Delta}.$$

By substituting (1.9) into (1.8), and integrating with respect to Δ, a first order ODE in E, with Δ, rather t, as variable is obtained:

$$E(\Delta) = \frac{\sqrt{2}}{\epsilon}\left(\frac{1}{2}(1-g_mR)\Delta^2 + \frac{1}{32}\Delta^4\right). \tag{1.9}$$

[11] identifies $\frac{dE}{d\Delta}$ as a gradient vector field, i.e., the vector field (RHS of eq.(1.8)) that guides the equation of motion, is the gradient of a scalar valued function representing the potential field, E. However, [11] does not elaborate on any further physical meaning on the potential field.

[1] In [11], the normalized current is denoted as z

Chapter 2

Identification of the Potential Energy of the Schmitt Trigger

The Schmitt trigger is an important component in many electronic circuits such as astable multivibrators/relaxation oscillator, monostable multivibrators, comparators, sense amplifier/flip flop/cross coupled inverter pair [14][18][19][20][21][22]. When applying bistable circuit to systems where metastability is of consideration, as for example, being sense amplifier in memory, being cross coupled inverter pair for entropy source in True Random Number Generator (TRNG), it turns out basing the analysis on energy, rather than voltage and current of the circuit, is more fruitful. [14] illustrates qualitatively the bistable system such as Schmitt trigger to a physical analog as ball rolling from top to bottom of a hill as shown in Figure 2.1. The system exhibits metastability when the ball is resting at the top i.e. highest potential energy. A small disturbance on the ball causes the ball to roll down the hill and settles at the stable states, the lowest potential energy. A first attempt on analyzing this metastability is given in [11]. [11] interprets the potential from the point of view of the gradient vector field. This is more a nonlinear dynamic system approach [12]. The potential energy is given a physical meaning as electrostatic energy, analogous to potential energy of the ball on top of a hill. This is used to show that, the metastability condition, corresponding to the highest potential energy, through regeneration, will have the system's energy lowered to the minimum energy, and settle to a stable condition. Note, the application of variational principle, or minimizing of energy has also been recently applied in the circuit community for other applications [13].

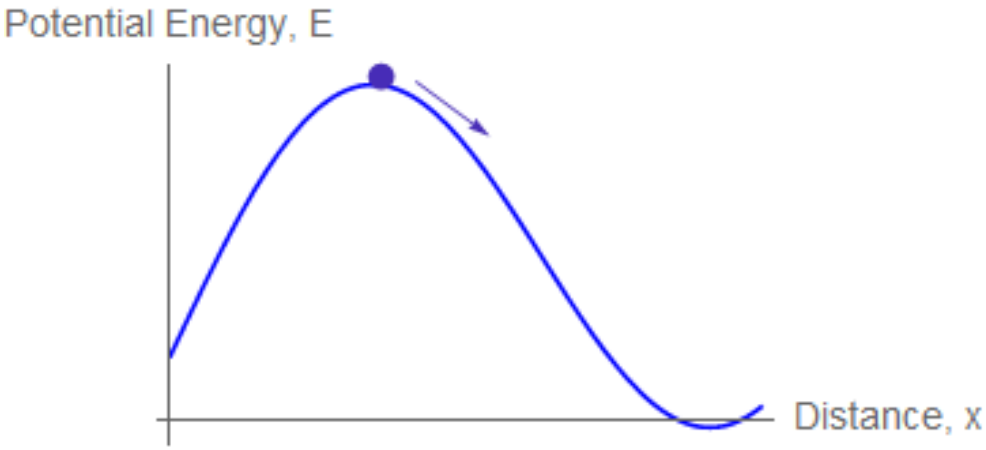

Figure 2.1: Potential Energy, E vs Distance, x. It illustrates the particle (round ball) always move "downhill" and settles to a position with the least potential energy along its trajectory

2.1 The Dynamic Equations of Schmitt Trigger

The physical interpretation of 'E' is performed by analysing the macroscopic behaviour of the Schmitt trigger. Method 1 from Table 1.1 is implemented in this chapter by assuming that the system can be represented by one degree of freedom (i.e. the coordinate is the normalized current). The Schmitt trigger has both C_{gs1} and C_{gs2} included, as shown in Figure 1.5. The design parameters of the circuit are set to be $R_1 = R_2 = R$, $k_{n1} = k_{n2} = k_n$ and λ=1.

The circuit is now described by two (rather than one) coupled first order differential equations, with both C_{gs1} and C_{gs2} included, which is not done in [11]. By applying KCL at the drain nodes of both M_1 and M_2, (2.1), (2.2) and (2.3) are obtained:

$$\begin{aligned} i_{Cgs1} &= i_{R2} - i_{d2} && (2.1)\\ i_{Cgs2} &= i_{R1} - i_{d1} && (2.2)\\ I_0 &= i_{R1} + i_{R2}. && (2.3) \end{aligned}$$

Next applying KVL around the loop of resistors, R_1, R_2, and transistors, M_1, M_2, it gives:

$$i_{R2} - i_{R1} = \frac{v_{gs2} - v_{gs1}}{R}. \quad (2.4)$$

By symmetrizing around the common mode signal, $\frac{I_0}{2}$, i_{R1} and i_{R2} are obtained:

$$i_{R1} = \frac{I_0}{2} - \frac{v_{gs2} - v_{gs1}}{2R} \tag{2.5a}$$

$$i_{R2} = \frac{I_0}{2} + \frac{v_{gs2} - v_{gs1}}{2R}. \tag{2.5b}$$

The capacitor current,i_{Cgs1} and i_{Cgs2}, are related to voltage, v_{gs1}, v_{gs2} respectively as shown below:

$$i_{Cgs1} = C_{gs1}\frac{dv_{gs1}}{dt} \tag{2.6a}$$

$$i_{Cgs2} = C_{gs2}\frac{dv_{gs2}}{dt}. \tag{2.6b}$$

Transistor device equations using long channel approximation (ie. square law) give

$$v_{gs1} = \sqrt{\frac{2i_{d1}}{k_n}} + v_t \tag{2.7a}$$

$$v_{gs2} = \sqrt{\frac{2i_{d2}}{k_n}} + v_t. \tag{2.7b}$$

The current flowing through the transistors, i_{d1} and i_{d2} can be related to the capacitor voltage, v_{gs1} and v_{gs2} :

$$\frac{di_{d1}}{dt} = \sqrt{2k_n i_{d1}}\frac{dv_{gs1}}{dt} \tag{2.8a}$$

$$\frac{di_{d2}}{dt} = \sqrt{2k_n i_{d2}}\frac{dv_{gs2}}{dt}. \tag{2.8b}$$

By substituting (2.5)-(2.8) into (2.1) and (2.2), two coupled differential equations are obtained as shown in (2.9a) and (2.9b):

$$C_{gs1}\frac{di_{d1}}{dt} = \sqrt{2k_n i_{d1}}\left(\frac{I_0}{2} + \frac{1}{2R}\left(\sqrt{\frac{2i_{d2}}{k_n}} - \sqrt{\frac{2i_{d1}}{k_n}}\right) - i_{d2}\right) \tag{2.9a}$$

$$C_{gs2}\frac{di_{d2}}{dt} = \sqrt{2k_n i_{d2}}\left(\frac{I_0}{2} - \frac{1}{2R}\left(\sqrt{\frac{2i_{d2}}{k_n}} - \sqrt{\frac{2i_{d1}}{k_n}}\right) - i_{d1}\right). \tag{2.9b}$$

Then, the phase portrait of an example of bistable system described in (2.9) is plotted in Figure 2.2. It shows that the Schmitt trigger has 1 metastable state at $\left\{\frac{i_{d1}}{I_0}, \frac{i_{d2}}{I_0}\right\} =$

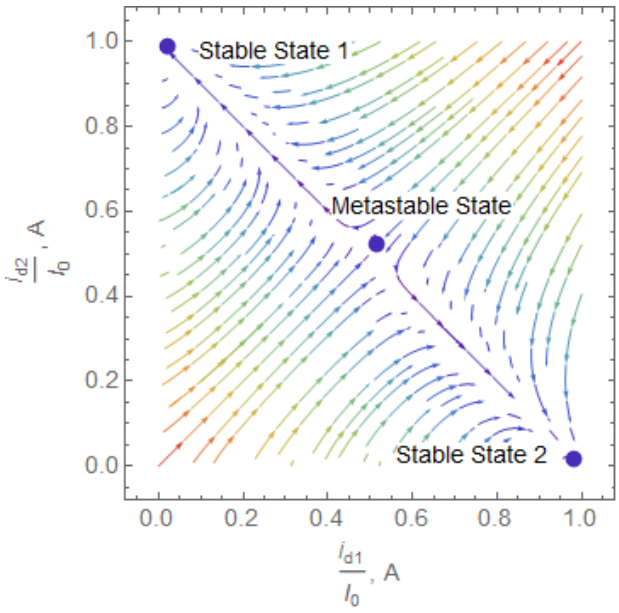

Figure 2.2: Phase Portrait of (2.9a), (2.9b) using Normalized Currents, $\frac{i_{d2}}{I_0}$ vs $\frac{i_{d1}}{I_0}$

$\{0.5, 0.5\}$ and 2 stable states at $\left\{\frac{i_{d1}}{I_0}, \frac{i_{d2}}{I_0}\right\} = \{0, 1\}$ and $\left\{\frac{i_{d1}}{I_0}, \frac{i_{d2}}{I_0}\right\} = \{1, 0\}$. At the metastable state, $i_{d1} = i_{d2} = \frac{I_0}{2}$. With some disturbance (noise) to the system, the system will settle to the stable states. Hence it behaves like a 2 level system. It is also shown that the dynamics of the system is symmetrical at $i_{d1} = i_{d2}$.

Figure 2.3 shows the phase curve of the system going down from either side of the metastable state. As shown in Figure 2.3, the system trajectory either moves toward the stable state, , $\left\{\frac{i_{d1}}{I_0}, \frac{i_{d2}}{I_0}\right\} = \{0, 1\}$ or moves toward the stable state, $\left\{\frac{i_{d1}}{I_0}, \frac{i_{d2}}{I_0}\right\} = \{1, 0\}$. The time evolution of the normalized currents, $\frac{i_{d1}}{I_0}, \frac{i_{d2}}{I_0}$ for the case of Figure 2.3a is shown in Figure 2.4.

2.2 The Potential Energy of Schmitt Trigger

To obtain the potential energy, the development of the dynamics is pushed even further. The co-ordinates are transformed, such that in this transformed co-ordinate system, the resulting ODE has a similar form as that of some familiar physical system (such as forced spring/pendulum), which:

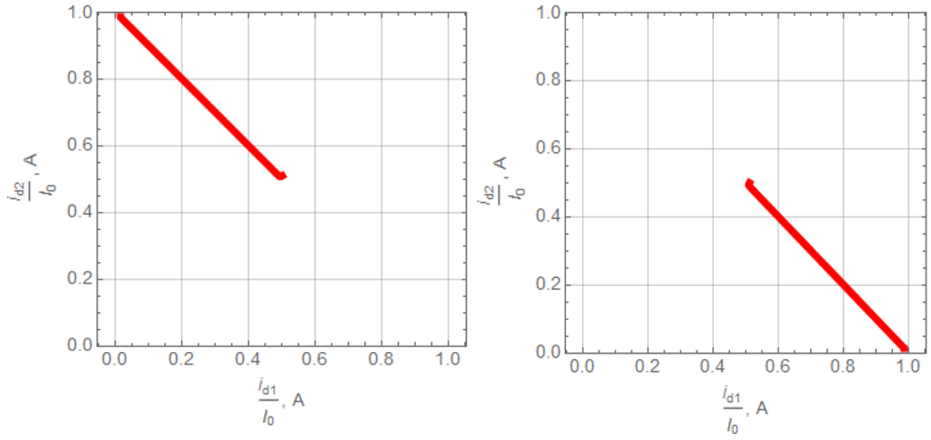

Figure 2.3: Phase curve of normalized Currents, $\frac{i_{d2}}{I_0}$ vs $\frac{i_{d1}}{I_0}$ (a) Red line is the trajectory of the Schmitt Trigger when the system dynamic moves from metastable state to stable state 1, (b) Red line is the trajectory of the Schmitt Trigger when the system dynamic moves from metastable state to state 2.

a) Behaves as a 2 level system

b) have well known expression for potential energy.

By comparing the ODE describing the bistable Schmitt trigger in this transformed co-ordinate to that of the physical system, proper mapping can be established, which can be carried over to the energy expression.

To obtain the ODE in transformed co-ordinate, (2.9b) is subtracted from (2.9a), and (2.10) is obtained. Then by setting $C_{gs1} = C_{gs2} = C_{gs}$ and replacing both $\sqrt{2k_n i_{d1}}$ and $\sqrt{2k_n i_{d2}}$ by the same term $\sqrt{2k_n \frac{I_0}{2}}$=$\sqrt{2k_n I_0}$=$g_m$[1] and it gives:

$$\frac{C_{gs}}{g_m}\frac{d(i_{d1}-i_{d2})}{dt} = \frac{1}{R}\left(\sqrt{\frac{2i_{d2}}{k_n}}-\sqrt{\frac{2i_{d1}}{k_n}}\right)+i_{d1}-i_{d2}. \tag{2.10}$$

The normalized differential mode signal (common mode signal already given as $\frac{I_0}{2}$ before

[1]This is the transconductance of the transistors at metastable state, when the current flowing through the transistor is equal, $\frac{I_0}{2}$. It is assumed that the change of transconductance is negligible near the metastable state.

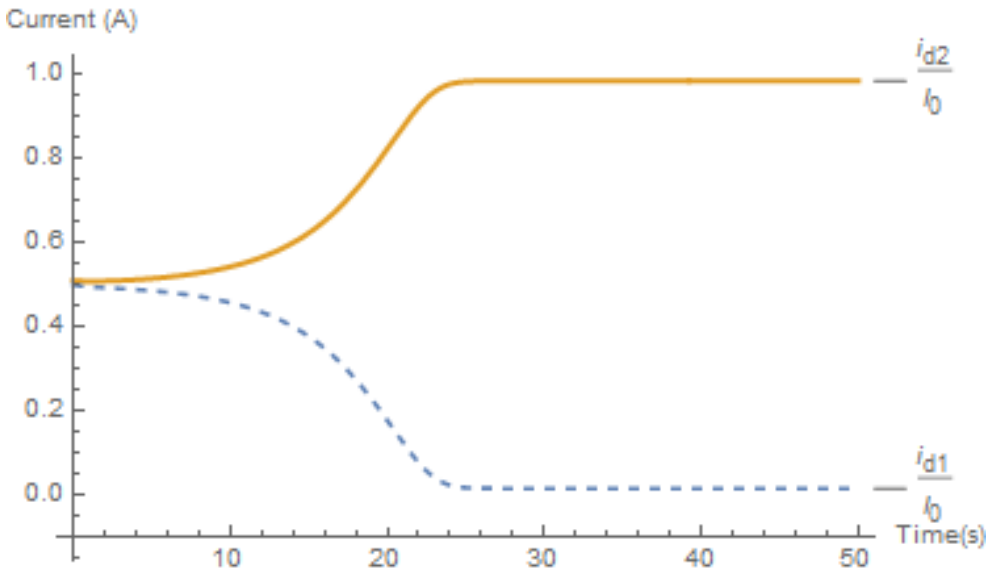

Figure 2.4: Time evolution of Current, $\frac{i_{d1}}{I_0}$ & $\frac{i_{d2}}{I_0}$ vs time, t

(2.5)), $\Delta = \frac{i_{d1}-i_{d2}}{I_0}$ is substituted into (2.10) to yield (2.11):

$$\frac{C_{gs}}{g_m}\frac{d\Delta}{dt} = \frac{-1}{Rg_m}\left(\sqrt{1+\Delta}-\sqrt{1-\Delta}\right)+\Delta. \tag{2.11}$$

(2.11) By using Taylor expansion at =0, $\sqrt{1+\Delta}-\sqrt{1-\Delta} = \Delta + \frac{1}{8}\Delta^3$. Then, (2.11) can be approximated to

$$RC_{gs}\frac{d\Delta}{dt} = (Rg_m - 1)\Delta - \frac{1}{8}\Delta^3. \tag{2.12}$$

Now lets turn to familiar physical system, "ball on the hill"/spring/pendulum (2 level mechanical system). For a damped spring system (where viscous damping force much stronger than the inertia term), having a nonlinear force, $F(x) = k_1x + k_2x^3$, the system is described as[17]:

$$\alpha\dot{x} = k_1x + k_2x^3. \tag{2.13}$$

α is friction coefficient, k_1, k_2 are the stiffness coefficients, while x is position. Comparing (2.12), (2.13), both have similar forms. However the spring system has familiar formula

for the potential energy, given as the integral on the right hand side (RHS) of (2.13):

$$\begin{aligned} E &= \int k_1 x + k_2 x^3 dx \\ &= \frac{1}{2} k_1 x^2 + \frac{1}{4} k_2 x^4 + Const_{spring}. \end{aligned} \tag{2.14}$$

Therefore, it is then led to integrate the RHS of (2.12), and interpret the result as the 'potential energy' of the Schmitt trigger, with the provision of 1) scaling of C_{gs} and 2) in $\frac{I_0}{g_m}$ in the variable:

$$E = -\frac{1}{C_{gs}} \left(\frac{Rg_m - 1}{2} \left(\frac{\Delta . I_0}{g_m} C_{gs} \right)^2 - \frac{1}{32} \left(\frac{\Delta . I_0}{g_m} C_{gs} \right)^4 \right) + Const. \tag{2.15}$$

E has unit of Joule. Moreover the potential energy of (2.15) is an even function, with 1 maximum, and sandwiched between two minima, another characteristic of a 2 level system.

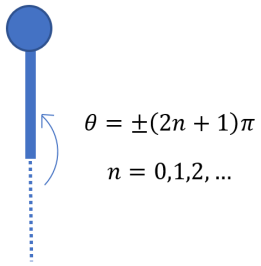

Figure 2.5: Inverted Pendulum System as 2 Level System

To visualize this better, instead of spring system, an inverted pendulum as shown in Figure 2.5 (with weight at the top, resting on a rod) is used for illustration. It is at the metastable state, with maximum energy, and any perturbation push it to the stable state. Again the potential energy versus position is like (2.15). We now normalize (2.15) by having $\frac{I_0}{g_m} = 1$ and $C_{gs} = 1$. This gives

$$E_{normalized} = -\frac{Rg_m - 1}{2} \Delta^2 + \frac{1}{32} \Delta^4 + Const. \tag{2.16}$$

Now, the interpretation of (2.16) is interpreted using this energy perspective. Here, Δ, identified earlier as the normalized differential current (see (2.11)), is now viewed as as a

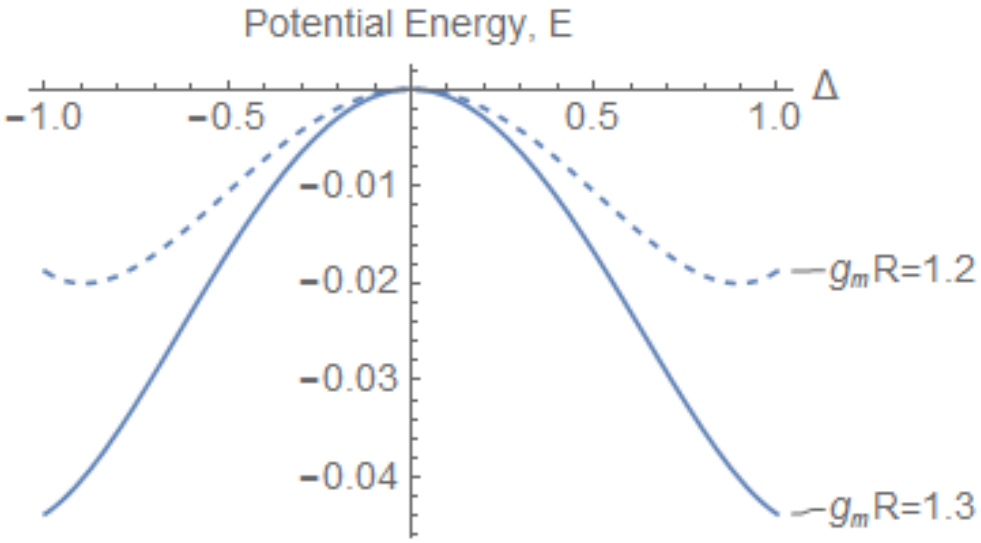

Figure 2.6: Potential Energy, $E_{normalized}$ vs Δ for parameter R=5kΩ, Const=0. The dashed line is with the parameter g_mR=1.2, and the solid line is with the parameter g_mR=1.22

transformed coordinate [23] of the voltage and v_{gs1}, v_{gs2} i.e. Δ is an algebraic function of v_{gs1}, v_{gs2}, such that $\Delta(v_{gs1}, v_{gs2}) = \frac{i_{d1}-i_{d2}}{I_0} = \frac{g_m}{I_0}(v_{gs1} - v_{gs2})$. By substituting $\Delta(v_{gs1}, v_{gs2})$ into (2.11), this gives the first term of (2.11) to be proportional to $\frac{1}{2}C_{gs}(v_{gs1} - v_{gs2})^2$, the differential electrostatic potential energy of transistor M_1 and M_2.

Now, first on the RHS of (2.11), the square root operates on this Δ, which reflects the nonlinearity of square law in the long channel I-V characteristic of M_1 and M_2. Secondly, the "$+\Delta$" and "$-\Delta$" terms inside the square root on the RHS of (2.11) reflects the coupling interaction across M_1 and M_2. These translate, upon Taylor expansion, into the linear and cubic term i.e. Δ, Δ^3 terms in (2.12), and subsequently, upon integration into the potential energy E, as Δ^2, Δ^4 terms in (2.16). In summary, E in (2.16) is rooted in V_{gs1}, V_{gs2}, (the coordinate in electrostatic potential energy), just like E in (2.14) is rooted in x, the co-ordinate in mechanical potential energy of the spring system. The definition of Const is the sum potential energy of the parasitic capacitors (in transformed co-ordinate) at the metastable state. (2.16) is then normalized [2] by setting Const to 0 and so that $E = 0$ at metastable state. Figure 2.6 shows that the potential energy of the Schmitt

[2]This is like the potential energy of a test charge q for a given charge, Q: when q is far away(∞ distance) from Q, the potential energy is zero and is at its maximum. When the charge q closes in, the electrostatic attraction causes the potential energy to be negative

trigger is maximum (E=0) at metastable state. When the bistable system reach its stable states, the potential energy is at its minimum (E<0). $\delta E = E_{meta} - E_{stable}$ is the difference between the potential energy of the metastable state, E_{meta} and the potential energy at stable states. E_{stable}. This can be derived by differentiating (2.16) with respect to Δ and setting it to 0, i.e., $\frac{dE}{d\Delta} = 0$. Then, the resulting $\Delta \left(\Delta|_{\frac{dE}{d\Delta}=0}\right)$ is substituted back into (2.16), giving expression for both E_{meta} and E_{stable}. This gives δE to be

$$\delta E = \frac{1}{2}(g_m R - 1)^2. \tag{2.17}$$

It shows that when $g_m R \to 1$, E goes to zero and the system behaves less and less like a 2 level system, and hence will not work as an effective Schmitt trigger. This is evident in Figure 2.6, when is lowered from 1.22 (solid line) to 1.2 (dash line), E is smaller.

The limitation of using the potential energy as an energetic theoretic method is that the internal degree of freedom of the system is neglected. The individual co-ordinate, i.e. the energy levels which the individual charges occupied has not been taken into full consideration. In the next chapter, all degree of freedom is included by considering the configurations in which these degree of freedom are distributed over energy levels. In essence the potential energy of the system is refined and generalized to the free energy of the system, which manifests in its dependency on temperature.

Chapter 3

The Free Energy Derivation of Schmitt Trigger

To include the internal degree of freedom for the system, method 2 of Table 1.1 is implemented by first looking into the microscopic picture of the system, is analysed. We start from obtaining the Hamiltonian and partition function of the system, and obtain the free energy from the partition function. Then, the statistical fluctuation of the system near the metastable state can be obtained from the free energy of the system. Schmitt trigger in Figure 1.5 is constructed to be source-coupled pair transistors with tail current. The internal mechanism of the pair transistors can be pictorially depicted as shown in Figure 3.1.

The circuit has a symmetrical construction of transistor M_1 and transistor M_2. Thermodynamically, the charges on the top plates of the two parasitic capacitors of M_1 (M_2), C_{gs1} (C_{gs2}) are represented as two ensembles in thermal equilibrium with one another, with the resistors acting as the heat reservoir, or heat bath. The charges of the both ensembles are charges stored in the parasitic capacitors (C_{gs1}, C_{gs2}). The number of charges for ensembles 1(2) is denoted as $N_1(N_2)$. The positive charges at the top plates of the parasitic capacitors is proportional to the number of electrons in the channel formed between the drain and source of the MOSFETs. In Figure 3.1, the positive charges are represented by filled plus and striped plus, while the electrons in the channel are represented by filled circles and striped circles.

The current flowing through the channel in M_1 is proportional to the number of electrons in the channel, i.e., $i_1 = WQ_Iv_d$ where Q_I is the total charges per area and v_d is the drift velocity of the electrons in the channel. Since $i_1 + i_2 = I_0$, the total number of

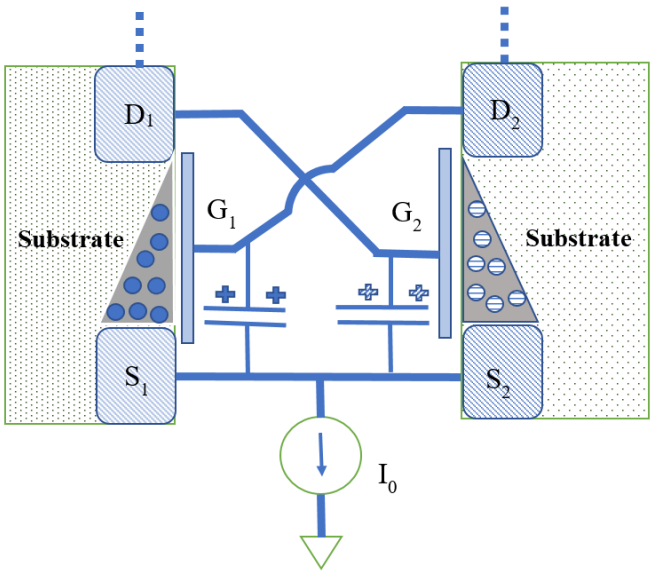

Figure 3.1: The ensemble of the system consist of charges on the parasitic capacitors(filled plus and striped plus).

charges in both channels is constant. I_0 defines the system size. It is assumed that the new electrons entering the channel are identical to the electrons flowing out from the channel to the source of the transistor.

Having a net negative charges in the channel between drain and source of the transistor causes the same net positive charge to collect on the gate of the transistor. Since the electrons in the channel of both transistors are conserved, the total charges on top of both parasitic capacitors top plate is conserved. The total number of charges is

$$N = N_1 + N_2. \tag{3.1}$$

where N_1 is the number of charges on the top plate of C_{gs1} and N_2 is the number of charges on the top plate of C_{gs2}.

In general the ensemble of a thermodynamic system is the mental collections of many copies of the same bulk system, with the macroscopic constraints defined through the parameters N and T, but existing in all different possible microstates/configurations. The total charge of the system is conserved since the tail current is assumed to be constant. Specifically for our thermodynamic system, the Schmitt trigger, the interaction energy is identified to be the change of energy of adding an electron in the channel of M_1 and removing a charge from the channel of M_2.

3.1 The Quantitative Description of Schmitt Trigger Interaction Energy, J with Macroscopic Transport Parameters Identified

To calculate the interaction energy, which is due to transfer of charge between M_1, M_2, let us start by considering the change of charges in transistor M_1 and M_2, involved in this transfer. From simple capacitor consideration i.e. Q=CV, the charges of transistor M_1 are

$$\begin{aligned} Q_1 &= C_{ox}(WL)(V_{ds2}) \\ &= C_{ox}(WL)(V_{gs1}). \end{aligned} \tag{3.2}$$

where C_{ox} is oxide capacitance per unit area and W, L are width and length of transistor M_1, and V_{ds2} is the voltage experienced by the charge. Because of the cross-coupling topology between the transistors M_1 and M_2, the drain-to-source voltage of transistor M_2 equals to the gate-to-source voltage of transistor M_2, i.e., $V_{ds2} = V_{gs1}$. Let us assume, with regeneration, $M_{1(2)}$ regenerate, i.e., the charge is pumped in/out with $\delta Q_{1(2)}$, the resulting change in voltage $\delta V_{gs1(gs2)}$ is:

$$\delta V_{gs1} = \frac{1}{C_{ox}(WL)}\delta Q_1 \tag{3.3}$$

$$\delta V_{gs2} = \frac{1}{C_{ox}(WL)}\delta Q_2. \tag{3.4}$$

With the tail current source feeding into both M_1, M_2, at any time interval, removal of charge from one transistor, is balanced by addition of equal amount of charge in the other transistor[1]. So, the change of charges in transistor M_1 is balanced by the opposite change of charges in transistor M_2 such that

$$\delta Q_1 - \delta Q_2 = 0. \tag{3.5}$$

Charges, of the drain currents i_{d1}, i_{d2} that travel through the transistors, experience potential $V_{ds1(2)}$, which due to cross coupling equal to $V_{gs2(1)}$. With the change of charge in M_1, the resulting change in energy is

$$\delta V_{ds1}\delta Q_1. \tag{3.6}$$

[1] this is assuming a) $i_{tail} = i_{d1} + i_{d2} + i_{cgs1} + i_{cgs2} \approx i_{d1} + i_{d2}$ (neglecting i_{cgs1}, i_{cgs2} which equal $C_{gs1}\frac{dv_{gs1}}{dt}$, $C_{gs2}\frac{dv_{gs2}}{dt}$ as i_{d1},i_{d2} changes slowly at beginning of regeneration, $C_{gs1}\frac{dv_{gs1}}{dt}$, $C_{gs2}\frac{dv_{gs2}}{dt} \approx 0$. Then $i_{d1} = -i_{d2}$ or $\delta Q_1 = -\delta Q_2$, with the presumption that the δQ_1, δQ_2, happens slowly, so that it is consistent with $C_{gs1}\frac{dv_{gs1}}{dt}$, $C_{gs2}\frac{dv_{gs2}}{dt} \approx 0$.

The symmetric construction of the Schmitt trigger circuit allows δV_{ds1} to be related to δQ_2 as shown below:

$$\begin{aligned} \delta V_{ds1} &= -\left(g_m R\right)^2 \delta V_{gs2} \\ &= -\left(g_m R\right)^2 \frac{\delta Q_2}{C_{ox} W L}. \end{aligned} \tag{3.7}$$

By substituting eq (3.7) to eq (3.6), the change in energy is

$$-\frac{\left(g_m R\right)^2 \delta Q_2 \delta Q_1}{C_{ox}(WL)}. \tag{3.8}$$

Note in the Schmitt trigger circuit this change in energy, is coupled between the charges of the 2 parasitic capacitors. The charges are

1. not physically transferred; rather one is delivered from ground via the current source, while the an equal amount is removed to ground by the same current source
2. the charge was original provided through the resistor, or heat reservoir.

In the special case when $\delta Q_1 = e$ and $\delta Q_2 = -e$, this change of energy in the interaction operation, is interpreted as the interaction energy, J. For introduction of a negative charge in transistor M_1 and removal of a negative charge in transistor M_2, the change of energy is given as

$$\begin{aligned} \delta E &= -\frac{\left(g_m R\right)^2 (+e)(-e)}{C_{ox}(WL)} \\ &= \frac{\left(g_m R\right)^2 e^2}{C_{ox}(WL)}. \end{aligned} \tag{3.9}$$

Now, the term $\frac{e}{C_{ox}WL}$ in (3.9) is identified to be the the electric potential experienced by the charge going through the virtual transfer for this specific case. It is then generalized to V_{peak}, where $V_{peak} = V_{gs1} - V_{gs2}$ and so the interaction energy is

$$J = \left(g_m R\right)^2 e V_{peak}. \tag{3.10}$$

Hence, the macroscopic transport parameter g_m, R, used to described J, have been identified.

3.2 The Hamiltonian (Semi-Microscopic) and Interaction Potential J of Schmitt Trigger

We adopt a semi-microscopic approach whereby the Hamiltonian of the system is simplified to illustrate only the essential features of this J potential interaction energy (between capacitor/cross-coupled pair part of the system, henceforth denoted as H), which encapsulates the microscopic behavior. Meanwhile, the transport behavior, derived from the Hamiltonian (of the transistor and resistor component of the system) is encapsulated in the macroscopic transport parameters, such as g_m, R. We will next go into microscopic details of Hamiltonian, which depends on the microscopic details of J.

With the considerations above, the Hamiltonian is given as below such that q_i is the occupancy of electrons at energy level i and q_j is the occupancy of electrons at next energy level, j:

$$\mathcal{H}(q) \quad = \quad -\mathcal{E}\sum_{i}^{N} q_i - \frac{1}{2}\sum_{\langle ij \rangle} J q_i q_j. \tag{3.11}$$

with q is the configurations of the system such that $q = \{q_1, q_2, ..., q_i, q_j, ...q_N\}$ and $\mathcal{E}$ [2] is the magnitude of electric field subjected to the individual charges. The notation $\langle ij \rangle$ indicates the adjacent/neighboring pairs of the energy levels. $q_i = 1$ when an electron occupies energy level i; $q_i = 0$ when an electron occupies energy level i. The two terms can crudely viewed as follows: first term as 'self' energy and second term as 'potential' energy due to interaction of the 'neighboring' charge, neighboring being looked as one charge, begetting another via the cross coupled pair action.

Now, we will discuss about the three essential features of this J interaction energy model.

3.2.1 Feature A: The Energy Levels Representation of Microscopic Interaction Energy Model

It is identified that the interaction energy, J comes from the cross-coupled topology of the circuit.

To describe the origin of J microscopically, lets look at the case of a standalone semiconductor capacitor. The electrons on top plate of the capacitors are distributed over the

[2] $\mathcal{E}$ is approximated to be zero in the subsequent derivation of free energy

energy levels described by the Fermi Dirac statistic, centered around the Fermi energy, E_f, situating around the conduction band energy, E_c. There is no interaction energy between the different electrons occupying the different energy levels. Next, let's visualize this capacitor as capacitor C_{gs} of a standalone transistor, denoted as M_1, and the situation remains the same, i.e., there is no interaction energy between the electrons. Then, lets look at the situation where M_1 is cross-coupled with another transistor, denoted as M_2. If we start to put an extra electron to C_{gs} of M_1, where it will sit at one of the vacant energy levels (it should be noted, these are still eigenenergies, but corresponds now to Hamiltonian of the coupled system;) . The cross coupling will result in an extra extra electron, in another vacant energy levels, via the coupling/interaction energy, J.

The virtual transfer of an electron can be depicted in following simple example: first, an electron (lets denote it as e_1) travels through the transistor, M_1, through the resistor, R. It is then dumped on the top plate of the parasitic capacitor, C_{gs2} and occupy an energy level in the band structure. An equal and opposite charge is deposited on the bottom plate of C_{gs2}. Since the bottom plate of C_{gs1} and C_{gs2} are connected, the top plate of C_{gs1} loses an electron. Since the tail current is constant, a new electron, e_2 is deposited on the top plate of C_{gs2}. For simplicity, let us assume this occupies the next higher energy level (with thermal energy, this needs not be the case, and in general this occurs with the Fermi Dirac probability). The removal of an electron on the top plate of C_{gs1} is compensated by the addition of a new electron on the top plate of C_{gs2}, the electron is virtually transferred from transistor M_1 to transistor M_2. As illustrated above, the interaction energy accompanying the transfer virtual of electrons is independent of the physical location or placement of the charges (the charges are spread throughout the top plate of the capacitor in an arbitrary fashion; a particular charge needs not be spatially identified with specific site on the top plate, unlike spin in Ising model, where each spin is situated on a specific site [3]). Therefore, whereas, in Ising model, interaction energy is dependent on the distance (spatial) between sites), here, rather, the coupling, or interaction energy, between 2 charges (occupying two energy levels) is dependent on the distance (energy difference) between the 2 energy levels occupied . This is because different energy levels occupied result in different capacitor voltage, or V_{peak} in (3.10), (proportional to energy level), which in turn bias the transistor differently, resulting in different coupling strength of the cross coupling transistor pair.

[3] On the other hand, like Ising model, where one and only one spin occupies per site, here, assuming no degeneracy, one and only one electron occupies an energy level. It should be noted there are fewer electrons (these are excess electrons, due to charge on capacitor, and for our case is on the order a hundreds to thousands) than energy levels (correspond to energy levels in the conduction band of a doped silicon, the top plate of the capacitor)

3.2.2 Feature B: The Interaction Energy, J of the Nearest Neighbour

Using the J discussed above, for interaction potential among the electron ensembles on the capacitor in cross-coupled (Schmitt Trigger) system, we can describe the Hamiltonian of this ensemble. As discussed in the introduction, Table 1.1, in this section, we are content just to discuss the classical Hamiltonian (like Ising), and derive the resulting fluctuation, which of course is just valid in the classical, or high temperature regime. The Interaction energy, J, we discussed previously, rooted in a potential that is dependent on distance between energy level, is taken as a scalar, and therefore, the Hamiltonian is treated as a scalar valued function [4].

As an example, the coupling between the transistors, M_1 and M_2 is the strongest at metastable states, when both the transistors are on. When the system is at stable states, one of the transistors is off and there is no coupling between the transistors. The strength of coupling between the transistors depends on the resultant voltage biasing of the cross-coupled transistors. This is different from the interaction energy between spins of Ising model where the coupling between two spins is inversely proportional to the distance between the spins. The magnitude of interaction energy between the spins is distance dependent with only the nearest neighbour couplings of the spins being considered in the Hamiltonian for a simple Ising model. For Schmitt trigger, on the other hand, the coupling between the both transistors is voltage-biasing dependent. The voltage bias of the transistors depends on the average potential of a single charge. For example, on the top plate of parasitic capacitor, if an electron occupies the energy level, i and another electron occupy the energy level, k where the energy differences between i and k is large, the average potential of each electron decreases substantially.

For illustration, a simple example is shown in Figure 3.2. Starting from M_1, C_{gs1}, let us look at the ensemble of electrons, shown as ++. The occupancy of energy level is shown (again for simplicity, at T=0, where the lowest levels are occupied). Starting with the two lowest levels i.e. i=1,2. This set up the capacitor voltage, V_{Cgs1} and bias M_1. Through cross coupling via M_2 this will put more electrons on M_1. The next such electron (q_3) is on i=3, as shown because if we add electron, due to Pauli exclusion principle, it will occupy i=3. The resulting change in voltage is as given by (3.8) and the coupling strength J, as given by (3.10) will, if we consider only the nearest neighbor (like Ising model), lead to

[4] Strictly speaking, the energy levels i.e. energy eigenvalues stem from quantum mechanical treatment, while this chapter is on classical development. Thus, we are simply using the energy levels as an analog of the Ising lattice sites. In essence, we treat both of them as classical variables. There will be some discussion in Chapter 4 when we do quantum development.

Hamiltonian H in (3.11).

In the Ising model, the potential is smaller as the site index difference which the spins occupy increases. Similarly, here as the difference in energy levels which the electrons occupy increases, the potential decreases. The interaction energy, $J \propto V_{peak} \propto \sum_i \frac{E_i}{q_i}$ is proportional to the sum of the occupied energy levels, and dominated by the highest occupied energy level. When q_3 is added to the top plate of the capacitor, the interaction energy is dominated by q_3 and q_2, since q_2 occupies the higher energy level than q_1. For Ising model, the interaction energy between two spins is inversely proportional to the site index difference (i.e. the site index difference is larger, then interaction energy is weaker). Similarly, for our case, the electron that occupies the highest energy level (q_2 instead of q_1) has the strongest interaction energy with the coming electron (q_3). The difference in energy levels is equivalent to the difference in site index of Ising model. Electrons with adjacent energy levels dominate the interaction energy, just like the spin in neighbouring site has strongest interaction energy.

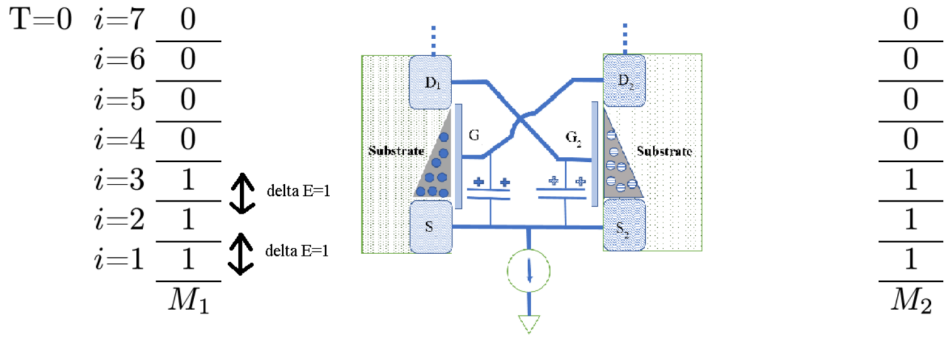

Figure 3.2: Microscopic example of interaction energy model

3.2.3 Feature C: The Configurations (Many Degree of Freedom Arising from Temperature) of the Ensemble

Next, the ensembles, unlike in Chapter 2 which gives one degree of representation for the entire ensemble, resulting in a potential E, now is going to possess many degrees of freedom, one for each configuration. As an example, using 1-dim representation, with an ensemble of N charges, the configuration is designated as $q = \{q_1, q_2, ..., q_i, q_j, ...q_N\}$ distributed over the energy levels E_1, E_2,...,E_i, E_j,...E_N. We define q_i to be the occupancy of charge in energy level i and q_j to be the occupancy of charge in the next higher energy level, j. These charges

are all going to be occupying starting from E_c, which equals E_f (assuming at regeneration, capacitor has no energy storage, ie. no offset of $\frac{1}{2}CV^2$ from E_c or E_f). So, the first charge occupies the ground state, E_f, and the next charge, by Pauli exclusion principle (assume no degeneracy),occupies the next higher energy level. An example for the configurations of ensemble with N=6 and $N_1 = 3$ is shown in Figure 3.3. For this example, both transistors are on, and both have the same number of charges. Thus, they are biased at the same voltage. The Schmitt trigger is at metastable state. At temperature, $T = 0$, the charges occupy the lowest energy levels possible and there is only one possible configuration. At temperature, $T > 0$, there are many possible configurations with different energy level occupancy of the charges. The three configurations at M_1 shown in Figure 3.3 are as following: configuration 1: $q = \{1, 0, 0, 0, 1, 1, 0\}$; configuration 2: $q = \{0, 0, 1, 1, 1, 0, 0\}$; and configuration 3: $q = \{0, 1, 0, 1, 0, 1, 0\}$. These configuration corresponds to $N_1 = 3$.

T=0	i=7	0	0	T>0	0	0	0	0	0	0	
	i=6	0	0		1	1	0	1	1	0	
	i=5	0	0		1	0	1	1	0	1	
	i=4	0	0		0	1	1	0	1	1	
	i=3	1	1		0	0	1	0	0	1	
	i=2	1	1		0	1	0	0	1	0	
	i=1	1	1		1	0	0	1	0	0	
		M_1	M_2		M_1	M_2	M_1	M_2	M_1	M_2	
		(a)			(bi)		(bii)		(biii)		

Figure 3.3: At temperature $T = 0$, the charges occupy the lowest energy levels possible. At temperature $T > 0$, the occupancy of charges over the energy levels give various configurations of ensemble. Example of various ensemble configuration at metastable state with total number of charges,N=6 and N_1=3. The charges are distributed across the energy levels, E_i, with i indicates the energy level in the band structure of capacitor.

Next we go to the H given in (3.11) for each configurations. Configurations 1, 2, 3 have different Hamiltonian, and so when exponentiated, it refers to different probabilities (Boltzmann probability). For example (assuming J=1) configuration 1 energy is $q_5 \times q_6$ because there are 2 consecutive 1's and so J between 2 of them. q_1 is neglected because, as noted, the interaction energy between charges of non-adjacent energy level is not taken into account when summing $-Jq_iq_j$. We treat these energy, which is not adjacent, will result in the bias voltage of the transistor away from the metastable state (or regeneration point). The further away from the metastable state, the coupling of two transistors is

T=0	i=7	0	0	T>0	1	0
	i=6	1	0		0	0
	i=5	1	0		1	0
	i=4	1	0		1	0
	i=3	1	0		1	0
	i=2	1	0		1	0
	i=1	1	0		1	0
		M_1	M_2		M_1	M_2
		(a)			(b)	

Figure 3.4: Example of ensemble configuration at stable state with total number of charges,N=6 and N_1=6

weaker, and thus the interaction energy of two charges with non-adjacent energy levels is neglected. Thus, configuration 1 has energy -1J. Meanwhile, configuration 2 is $q_3 \times q_4 \times q_5$ because there are 3 consecutive 1s. Hence, the energy is -2J. In summary, configuration 1 and 2 have different energy, and so when weighed by β and taking exponential, it refers to different probabilities. Another example for the configurations of ensemble with N=6 and $N_1 = 6$ is shown in Figure 3.4. With $N_1 = 6$, transistor M_1 is on and transistor M_2 is off. Here, the Schmitt trigger is at stable state.

Next, lets define $\Delta = \frac{N_1 - N_2}{N}$ as a normalized order parameter. configurations with N_1 corresponds to a certain value of Δ. Using the example of Figure 3.3, the configurations at metastable state corresponds to $\Delta = 0$. The partition function, for a given Δ is as following:

$$\tilde{\mathcal{Z}}(\Delta) \quad = \quad \sum_{v} \Lambda(\Delta - \Delta_v) e^{-\beta E_v}. \tag{3.12}$$

where $\Lambda(\Delta - \Delta_v)$ is 1 when $\Delta = \Delta_v$ and 0 otherwise. The partition function, $\mathcal{Z} = \sum_{\Delta} \tilde{\mathcal{Z}}(\Delta)$ and $\frac{\tilde{\mathcal{Z}}(\Delta)}{\mathcal{Z}}$ is the probability for observing the system with order parameter Δ. For example, referring to Figure 3.3, for $T > 0$, $\tilde{\mathcal{Z}}(\Delta = 0) = e^{3\beta J} + e^{2\beta J} + ...$, with $e^{3\beta J}$ is the internal energy for configuration 1 of metastable state and $e^{2\beta J}$ is the internal energy for configuration 2 of metastable state. Another example for the configurations of ensemble with N=6 and $\Delta = 6$ is shown in Figure 3.4. With $\Delta = 6$, transistor M_1 is on and transistor M_2 is off. Then, the Schmitt trigger is at stable state. $\tilde{\mathcal{Z}}(\Delta = 1) = e^{5\beta J} + ...$, with $e^{5\beta J}$ is the internal energy for stable state at $T > 0$.

The number of configurations for metastable state is larger than the configurations for stable state. Referring to the example in Figure 3.3, the numbers of possible configuration

for metastable state ($T > 0$) are $\frac{7!}{3!\times 4!}$, while the number of possible configuration for stable state ($T > 0$) are $\frac{7!}{6!1!}$. The entropy, $S = kln(\Omega)$, with k is the Boltzmann constant and Ω is the number of configurations. So, The entropy is maximized at metastable state, since metastable state has the most number of configurations.

The total internal energy of the system is given [15] as

$$U = \frac{\sum_v E_v e^{-\beta E_v}}{\sum_v e^{-\beta E_v}}. \tag{3.13}$$

Using Figure 3.3 as an example, at metastable state ($T > 0$), the number of electron pair with adjacent energy levels (such that $q_i q_j = 1$) is one (configuration 2) or two (configuration 1) because the total charges in M_1 is 3. From equation, $U(\Delta = 0) = \frac{-Je^{J\beta}-2Je^{2J\beta}}{e^{J\beta}+e^{2J\beta}}$. Similarly, at stable state ($T > 0$), the number of adjacent occupied energy levels pair is either four or five. So, $U(\Delta = 1) = \frac{-4Je^{4J\beta}-5Je^{5J\beta}}{e^{4J\beta}+e^{5J\beta}}$. This gives $-2J < U(\Delta = 0) < -J$ and $-5J < U(\Delta = 1) < -4J$. To illustrate that, lets give a numerical example with $J = 1$ and $\beta = 1$. In this case, $U(\Delta = 0)$ is -1.73, and $U(\Delta = 0) = -4.73$. The total internal energy at stable states is always lower than the total internal energy at metastable state because the stable state has higher number of electron pair with adjacent energy levels. The free energy is given as $U - TS$. The metastable state has more free energy than the stable states given that $U(\Delta = 0) - TS(\Delta = 0) > U(\Delta = 1) - TS(\Delta = 1)$

3.3 The Free Energy of Schmitt Trigger

The existence of many configurations (many degree of freedom) at a finite temperature can physically be traced back to scattering that occurs to electrons in the ensemble when the electrons travels through the resistors during the virtual transfer. To capture quantitatively all these configurations, one resorts to the partition function to describe the system. As we want to center the metastable state at $\Delta = 0$, the following transformation is performed:

$$c_i = 2q_i - 1 \tag{3.14}$$

where $c_i = \pm 1$ and $q_i = 1, 0$. The partition function with no external electric field, $\mathcal{E}$, now a function of temperature, is given as the sum of all configurations of the system weighed with $\beta = \frac{1}{k_B T}$ as shown below:

$$\mathcal{Z}(N, T) = \sum_{c_1} \dots \sum_{c_N} e^{-\beta\left[-\frac{1}{2}\sum_{\langle ij\rangle} J_{ij} c_i c_j\right]}. \tag{3.15}$$

Here N, as defined before, is the number of charge in the ensemble, T is the temperature. The partition function is difficult to solve.Thus, mean-field approximation is used to simplify the equation. In chapter 2, Δ is defined to be the normalized current, $\frac{i_{d1}-i_{d2}}{I_0}$. Assume that all electrons have the same drift velocity, $\Delta = \frac{N_1-N_2}{N}$ where N_1 is the number of electrons at transistor M_1, N_2 is the number of electrons at transistor M_2 and N is the total number of electrons in M_1 and M_2. Then, we can denote N_1 to be the sum of the occupied energy levels of transistor M_1, and N_2 to be the sum of unoccupied energy levels of the transistor M_1. Thus, the parameter Δ can alternatively be defined as

$$\Delta = \frac{1}{N}\sum_{i=1}^{N} c_i. \tag{3.16}$$

Then, c_i can be written as

$$c_i = c_i - \Delta + \Delta. \tag{3.17}$$

Using the identity eq (3.17), q_i is substituted into the Hamiltonian with

$$\begin{aligned} c_i c_j &= (c_i - \Delta + \Delta)(c_j - \Delta + \Delta) \\ &= (c_i - \Delta)(c_j - \Delta) + \Delta(c_i + c_j) - \Delta^2. \end{aligned} \tag{3.18}$$

Under mean field approximation [24] the term $(c_i - \Delta)(c_j - \Delta)$ is neglected. The Hamiltonian can be approximated as

$$\frac{1}{2}\sum_{\langle ij\rangle} J_{ij} c_i c_j \approx -\frac{1}{2} N J \Delta^2 + J\Delta \sum_i c_i. \tag{3.19}$$

with J defined such as $\sum_{\langle ij\rangle} J = NJ$. N is the total number of charges on both the top plate of parasitic capacitors (C_{gs1} and C_{gs2}).

The partition function becomes

$$\mathcal{Z} = e^{-\frac{\beta N J \Delta^2}{2}} \left(2\cosh\left(\beta J \Delta\right)\right)^N \tag{3.20}$$

Then, the free energy G(N, $\mathcal{E}, T$) can be found as

$$\begin{aligned} G &= -\frac{1}{\beta}\ln \mathcal{Z}(N,T) \\ &= \frac{1}{2} J\Delta^2 - \frac{1}{\beta}\ln\left(2\cosh\beta J\Delta\right). \end{aligned} \tag{3.21}$$

To approximate the free energy, G at metastable state ($\Delta = 0$), we Taylor expand the second term of (3.21) such that $\ln(2\cosh\beta J\Delta)|_{\Delta=0} \simeq \ln(2) + \frac{(\beta J\Delta)^2}{2} - \frac{(\beta J\Delta)^4}{12} + \ldots$, then the result is

$$\frac{kT}{2}\left[\left(1 - \frac{(g_m R)^2 eV_{peak}}{kT}\right)\Delta^2 + \frac{\Delta^4}{6} + Const\right]. \tag{3.22}$$

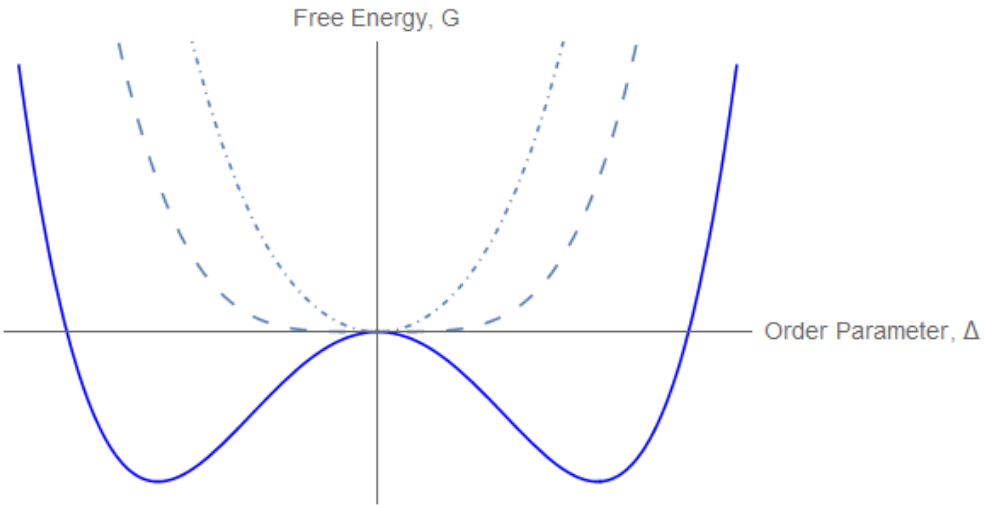

Figure 3.5: Free Energy vs Δ (Solid line: $g_m ReV_{peak} < kT$, Dashed line: $g_m ReV_{peak} = kT$, DashDotted line=$g_m ReV_{peak} > kT$)

Figure 3.5 indicates that the plot shows metastability when $(g_m R)^2 ReV_{peak} < kT$. When the temperature decreases, the energy difference between metastable state and stable states, decreases until a point where the metastability of the system vanishes. For the case of $(g_m R)^2 ReV_{peak} < kT$ where the metastability of the system exists, the energy difference, is found to be

$$\frac{3}{2}\left(1 - \frac{(g_m R)^2 ReV_{peak}}{kT}\right)^2. \tag{3.23}$$

When $(g_m R)^2 eV_{peak} < kT$, the free energy obtained is an even function, with two minimum points. This characteristic is similar to the potential energy obtained in section 2.2. However in section 3.3, it is made explicit that it comes from the circuit topology of the cross coupled pairwith the tail current source that we obtain the terms Δ^2 and Δ^4 in the end.

Using KCL on the cross couple pair gives us $\sqrt{1+\Delta}-\sqrt{1-\Delta}$ term that will be simplified to terms Δ^2 and Δ^4 by Taylor series approximations at $\Delta = 0$ (metastable state). The potential energy calculated in section 2.2 is compared with the potential energy of a ball rolling down the hill. The particles in the system are identified as a single entity that abide with the minimum energy principle. In this chapter, we introduce the randomness of the particles where the system has many energy configurations characterized by the thermal distribution. Summing up the energy of all configurations give us the free energy, in term of temperature. Both approaches show that the electronic bistable system has 2 stable states on either side of a metastable states.

3.4 The Normalized Current Fluctuation of Bistable Circuit

From the free energy of the system, the fluctuation of the normalized current, Δ is determined and is given by partial derivative of partition function with respect to the conjugate variable [5] as shown below:

$$\begin{aligned} \beta^2 N(\overline{\Delta^2} - \overline{\Delta}^2) &= \beta N \frac{\partial \bar{\Delta}}{\partial \mathcal{E}} \\ &= \frac{\partial^2}{\partial \mathcal{E}^2}(\ln \mathcal{Z}). \end{aligned} \tag{3.24}$$

The root-mean square fluctuation in normalized current, σ_Δ is defined as the square deviation of the normalized current, Δ from its mean value as shown below:

$$\sigma_\Delta = \sqrt{\overline{\Delta^2} - \overline{\Delta}^2}. \tag{3.25}$$

By substituting (3.24) into (3.25), σ_Δ can be represented as

$$\sigma_\Delta = \sqrt{\frac{\partial \bar{\Delta}}{\partial \beta \mathcal{E}}}. \tag{3.26}$$

From (3.22), Δ can be determined by requiring that it minimizes the free energy, that is, by setting $\frac{\partial G}{\partial \Delta} = 0$.

$$\begin{aligned} \frac{\partial G}{\partial \Delta} &= J\Delta - J\tanh(\beta J \Delta) \\ &= 0. \end{aligned} \tag{3.27}$$

[5] The conjugate variables are Δ and $\mathcal{E}$. Note that $\mathcal{E} \to 0$ doesn't mean that $\frac{\partial ln(\mathcal{Z})}{\partial \mathcal{E}} \to 0$

Then, a nonlinear equation for normalized current, Δ is obtained as shown below

$$\Delta \;=\; \tanh(\beta J\Delta). \tag{3.28}$$

Since $\tanh(x) \approx x - \frac{x^3}{3} + ...$, (3.28) can be approximated to be

$$\Delta \;\approx\; \beta J\Delta - \frac{1}{3}(\beta J)^3\Delta^3. \tag{3.29}$$

When $kT > J$, the only solution is $\Delta = 0$. The system is in disorder state and the mean of the normalized current is equal to zero. When $kT < J$, spontaneous symmetry breaking [24] occurs. There are two non-trivial solutions where the system spontaneously picks one of the stable states. Solving the cubic equation of (3.29), the non-trivial solution gives

$$\Delta \;\approx\; \pm\sqrt{3\left(1 - \frac{1}{\beta J}\right)}. \tag{3.30}$$

By taking partial derivative of (3.28) with respect to $\beta\mathcal{E}$, the following expression is obtained:

$$\begin{aligned}\frac{\partial\Delta}{\partial\beta\mathcal{E}} &= Sech(\beta J\Delta + \beta\mathcal{E})\left(1 + J\frac{\partial\Delta}{\partial\mathcal{E}}\right)\\ &= (1 - Tanh^2(\beta J\Delta + \beta\mathcal{E}))\left(1 + J\beta\frac{\partial\Delta}{\partial\beta\mathcal{E}}\right).\end{aligned} \tag{3.31}$$

Then, by substituting (3.28) into (3.31),

$$\frac{\partial\Delta}{\partial\beta\mathcal{E}} \;=\; \frac{1 - \Delta^2}{1 - \beta J(1 - \Delta^2)}. \tag{3.32}$$

By substituting (3.30) into (3.32), $\frac{\partial\Delta}{\partial\beta\mathcal{E}}$ can now be expressed in term of βJ,

$$\frac{\partial\Delta}{\partial\beta\mathcal{E}} \;=\; \frac{1 - 3\left(1 - \frac{1}{\beta J}\right)}{1 - \beta J\left(1 - 3\left(1 - \frac{1}{\beta J}\right)\right)}. \tag{3.33}$$

For $\beta J \to 1$ and the interaction energy, $J = (g_m R)^2 eV_{peak}$ as derived in (3.10),

$$\begin{aligned}\frac{\partial\Delta}{\partial\beta\mathcal{E}} &\approx \frac{5}{2(\beta J - 1)}\\ &= \frac{5}{2\left(\frac{(g_m R)^2 eV_{peak}}{kT} - 1\right)}.\end{aligned} \tag{3.34}$$

The root-mean square fluctuation in normalized current is thus,

$$\sigma_\Delta \quad \propto \quad \frac{1}{\sqrt{\frac{(g_m R)^2 e V_{peak}}{kT} - 1}}. \tag{3.35}$$

The equation (3.35) is the fluctuation model for a bistable circuit, such as Schmitt trigger. A relaxation oscillator consists of Schmitt trigger and timing elements such as capacitor and resistor. Referring to the Appendix B, the relaxation process has a fast time scale, governed by the dynamic of the Schmitt trigger, and a slow time scale, dictated by the timing capacitor. As the noise spikes occurs during the regeneration process of the fast time scale, we can approximate the fluctuation of the Schmitt trigger to be the same as the fluctuation of the relaxation oscillator.

Thus, in summary, the expression for root-mean square fluctuation in normalized current obtained in (3.35) is consistent with the fluctuation expression in [11]. Both the fluctuation models are obtained with the assumption that the system is in thermal equilibrium. The fluctuation model in [11] compares the equation of states between the vdw gas and the relaxation oscillator and maps the corresponding variables to find the fluctuation of current for the relaxation oscillator. However, the equation of states, like vdw gas, works with the average pressure, volume and density will miss the microscopic aspect of physic. By investigating the microscopic physics of the circuit, we are able to obtain the thermodynamic quantities such as the free energy of the system, and obtain fluctuation from first principle in physics. However, when the temperature goes down enough, the underlying physics in the above free energy derivation, i.e. classical, may become invalid as quantum noise might manifest. This is not taken account in the derivation of the fluctuation model in this section. Because of the difficulty of finding eigenenergy in an interaction system, (eigenfunction is needed in the generalization of the free energy calculation method to quantum case), such as the present relaxation oscillator, finding free energy is also difficult, as stated in table 2. Therefore, an alternative, namely, method 3 is next presented, as shown in Table 1.1 .

Chapter 4

Derivation of Fluctuation Including Quantum Noise (Energy-Time Uncertainty) in Relaxation Oscillator Using Langevin Equation

4.1 Introduction

Following table 1.1, the Langevin approach is attempted in this chapter. This approach is good for system which can be simply represented by 1 degree of freedom (macroscopic behavior), but this time the microscopic/internal degree of freedom is 'decoupled' and assumed to be represented by 'immersion' in a heat bath with many degree of freedom. Compared to *Method 2* presented in Chapter 3, instead of starting from the statistical representation of the system at thermal equilibrium, i.e. its free energy (and only the bistable part), and then obtain statistical properties of the system, such as the average and fluctuation of the normalized current, *Method 3* presented in this chapter first starts from equation of motion of the statistical representation i.e. $\rho(t)$ or density matrix. From $\rho(t)$ throughout the period/cycle, it then obtain the time properties, such as the average and fluctuation. Finally it equates the time property to the statistics properties, such as average and fluctuation of current, by employing the ergodic theorem. In Langevin approach, instead of looking at equation of motion of $\rho(t)$ directly, the statistical representation is split into two parts: i) deterministic part ii) noise source. Hence one needs to find i) the equation of motion of deterministic part ii) find the time average of the system

by integrating the noise part contribution along this equation of motion throughout the cycle/period. Thus equation of motion of the deterministic part of the system, namely, relaxation oscillator, and also throughout the whole cycle, needs to be obtained. It should be noted that, comparing to *Method 2*, now we look at not just the bistable circuit at the regeneration point, but also the whole relaxation oscillator, and through the rest of the cycle. Hence we would separate the whole cycle into a regeneration (fast) phase and a charging/discharging (slow) phase. The full explanation of the connection between two-phase model and relaxation oscillator is given in Appendix B.

4.2 Derivation of Energy Dissipated in Relaxation Oscillator at Metastable State

Following Appendix B, the noise is dominated by the fast phase of the oscillation period of relaxation oscillator. The deterministic equation of motion for fast phase is developed as below.

To find the equation of motion describing the system in the fast phase of oscillation, the circuit topology as shown in Figure 1.3 is analysed. The voltage across the capacitor, V_C defines the regeneration voltage. For simplicity, the voltage across capacitor, V_C is set to be zero. Next we linearize the circuit since we are interested only at the small region around the metastable state, when the fluctuation is the biggest. By using Kirchhoff's Voltage Law (KVL) around the loop of transistor M_1, M_2, an expression is obtained:

$$(i_1 - i_{cgs1})R + v_{gs2} - (i_2 - i_{cgs2})R - v_{gs1} = 0. \tag{4.1}$$

where $i_{1(2)}$ is the small-signal current flowing through the resistor, R; $v_{gs1(gs2)}$ is the small signal gate-to-source voltage of the transistor $M_{1(2)}$ and i_{cgs1} and i_{cgs2} are the displacement current. The gate-to-source voltage can be expressed in terms of current, such that $v_{gs1} = \frac{1}{g_m} i_1$ and $v_{gs2} = \frac{1}{g_m} i_2$ where g_m is the transconductance of transistor M_1 and M_2. Then, (4.1) can be expressed as

$$\frac{i_{cgs1} - i_{cgs2}}{g_m} = (i_1 - i_2)\left(R - \frac{1}{g_m}\right). \tag{4.2}$$

Next, the displacement current, $i_{cgs1} = \frac{C_{gs}}{g_m}\frac{di_1}{dt}$ and $i_{cgs2} = \frac{C_{gs}}{g_m}\frac{di_2}{dt}$. By substituting the displacement currents into (4.2),

$$RC_{gs}\frac{d(i_1 - i_2)}{dt} = (i_1 - i_2)(g_m R - 1). \tag{4.3}$$

Since $i_1 + i_2 = 0$, two differential equations can be obtained from (4.3):

$$\frac{di_1}{dt} = \frac{1}{2}(i_1 - i_2)\frac{g_m R - 1}{RC_{gs}} \tag{4.4}$$

$$\frac{di_2}{dt} = -\frac{1}{2}(i_1 - i_2)\frac{g_m R - 1}{RC_{gs}}. \tag{4.5}$$

By substituting (4.4) and (4.5) into (4.3), the second order differential equation of i_1, the current flowing through transistor, M_1 is obtained as below:

$$\frac{d_1^2 i}{dt^2} = \frac{1}{2}\frac{g_m R - 1}{RC_{gs}}\frac{di_1}{dt} + \frac{1}{4}\frac{(g_m R - 1)^2}{(RC_{gs})^2} i_1. \tag{4.6}$$

The small-signal voltage across the resistor $v_R = -i_1 R$,

$$\frac{d^2 v_R}{dt^2} = \frac{1}{2}\frac{g_m R - 1}{RC_{gs}}\frac{dv_R}{dt} + \frac{1}{4}\frac{(g_m R - 1)^2}{(RC_{gs})^2} v_R \tag{4.7}$$

To present (4.7) in a more elegant way, the damping coeficient, γ and the angular frequency, w_0 for the relaxation oscillator circuit are defined as

$$\gamma = \frac{g_m R - 1}{RC_{gs}} \tag{4.8}$$

$$w_0^2 = \frac{(g_m R - 1)^2}{(RC_{gs})^2}. \tag{4.9}$$

By substituting (4.8) and (4.9) into (4.7), the simplified 2^{nd} order differential equation is :

$$\frac{d^2 v_R}{dt^2} = \frac{1}{2}\gamma\frac{dv_R}{dt} + \frac{1}{4} w_0^2 v_R. \tag{4.10}$$

The solution for (4.10) gives voltage across the resistor. The energy δE dissipated due to current noise, $I_n(t)$ across the resistor is given by integrating the power, which in turn is given by the product of voltage v_R and noise current, I_n.

$$\begin{aligned} \delta E &= -\int_0^{T_0} v_R(t) I_n(t) dt. \\ \langle \delta E^2 \rangle &= \int_0^{T_0} dt \int_0^{T_0} \langle v_R(t) v_R(t') I_n(t) I_n(t') \rangle dt' \\ &\approx \int_0^{2T_f} dt \int_0^{2T_f} v_R(t) v_R(t') \alpha(t - t') dt' \end{aligned} \tag{4.11}$$

with $\langle I_n(t)I_n(t')\rangle \equiv \alpha(t-t')$. By integrating the dissipated power over the period of stable oscillation, it gives a time-averaging of the system in thermal equilibrium.[1]. The power dissipated in the period T_0 can be approximated to be the power dissipated during the time scale of the fast dynamic, T_f since the noise spike is generated during the fast time scale [2].The Fourier transform of eq (4.11) gives

$$\langle \delta E^2 \rangle = \frac{1}{2\pi}\int_{-\infty}^{\infty} d\omega |v_R(w)|^2 \alpha(w). \tag{4.12}$$

As $I_n(t)$ corresponds to colored Gaussian noise,

$$\begin{aligned} \langle I_n(t)I_n(t')\rangle &\equiv \alpha(t-t') \\ \alpha(w) &= \int_{-\infty}^{\infty} \exp(-i\omega t)\alpha(t)d\omega \\ &= \frac{\hbar w}{R}\coth\left(\frac{\beta\hbar w}{2}\right) \\ with\ \beta &= \frac{1}{kT}. \end{aligned} \tag{4.13}$$

By applying Fourier transform to the solution of 2^{nd} order differential equation, (4.10) and finding the magnitude square of the voltage in term of angular frequency, w is

$$|v_R(w)|^2 = C_1^2 \frac{1}{\gamma^2 + (w-w_0)^2}. \tag{4.14}$$

where C_1 is the initial voltage of the relaxation oscillator at metastable state where $C_1 = V_{peak}$. By substituting (4.13) and (4.14) into (4.12), the energy fluctuation is

$$\langle \delta E^2 \rangle = \frac{1}{2\pi}\int_{-\infty}^{\infty} d\omega V_{peak}^2 \frac{1}{\gamma^2 + (w-w_0)^2} \times \frac{\hbar w}{R}\coth\left(\frac{\beta\hbar w}{2}\right). \tag{4.15}$$

In high temperature regime, $\beta \to 0$. Then, it can be approximated such that $\coth\left(\frac{\beta\hbar w}{2}\right) \approx$

[1] From fluctuation dissipation theorem, this is interpreted as the fluctuation of the system

[2] The noise during the slow dynamic is $\frac{kT}{C}$ and is relatively smaller. Thus, the power dissipated $V \times I_n$ during slow phase, T_s is negligible. so integral of the power includes only the equation of motion of the fast phase.

$\frac{2}{\beta\hbar w}$. The $\hbar w$ got cancelled with the $\hbar w$ in $\frac{\hbar w}{R}$ in the integrand above.

$$\begin{aligned}
\langle \delta E^2 \rangle &= \frac{1}{2\pi}\int_{-\infty}^{\infty} d\omega V_{peak}^2 \frac{1}{\gamma^2 + (w - w_0)^2} \times \frac{\hbar w}{R}\left(\frac{2}{\beta\hbar w}\right) \\
&= \frac{V_{peak}^2}{\beta R\pi}\int_{-\infty}^{\infty} \frac{1}{\gamma^2 + (w - w_0)^2} \\
&= \frac{V_{peak}^2 kT}{R}\left(\frac{1}{\gamma}\right) \\
&= \frac{V_{peak}^2 kT}{R}\left(\frac{RC_{gs}}{Rg_m - 1}\right). \qquad (4.16)
\end{aligned}$$

In low temperature, $\beta \to \infty$, $\coth\left(\frac{\beta\hbar w}{2}\right) \to 1$.

$$\begin{aligned}
\langle \delta E^2 \rangle &= \frac{1}{2\pi}\int_{-\infty}^{\infty} d\omega V_{peak}^2 \frac{1}{\gamma^2 + (w - w_0)^2} \times \frac{\hbar w}{R} \\
&= \frac{\hbar V_{peak}^2}{2\pi R}\left[\frac{-w_0}{\gamma}\tan^{-1}\left(\frac{w_0 - w}{\gamma}\right) + \frac{1}{2}\log\left[\gamma^2 + (w_0 - w)^2\right]\right]_{w=-\infty}^{w=\infty}. \qquad (4.17)
\end{aligned}$$

The second term of (4.17) is approximated to be negligible since that,

$$\begin{aligned}
\frac{1}{2}\log\left[\gamma^2 + (w_0 - w)^2\right]_{w=-\infty}^{w=\infty} &= \frac{1}{2}\log\left[\frac{\gamma^2 + (w_0 - a)^2}{(\gamma)^2 + (w_0 + a)^2}\right]_{a\to\infty} \\
&\approx \frac{1}{2}\log(1) \\
&\approx 0.
\end{aligned}$$

As the second term of (4.17) is negligible,

$$\begin{aligned}
\langle \delta E^2 \rangle &= \frac{\hbar V_{peak}^2}{2\pi R}\left[\frac{-w_0}{\gamma}\tan^{-1}\left(\frac{w_0 - w}{\gamma}\right)\right]_{w=-\infty}^{w=\infty} \\
&= \frac{\hbar\omega_0 V_{peak}^2}{2R}\left(\frac{RC_{gs}}{Rg_m - 1}\right). \qquad (4.18)
\end{aligned}$$

The expression of fluctuation in energy of the system is obtained. Next, we attempt to acquire the fluctuation of current from (4.18). In thermodynamic system, the fluctuation

of energy is given such that [15] [3]

$$\langle \delta E^2 \rangle = kT^2 C_v + kT \left(\frac{\partial U}{\partial N} \right)_{T,V} \left(\frac{\partial U}{\partial \mu} \right)_{T,V}. \tag{4.19}$$

where μ is the chemical potential, N is the number of particles (charges), U is the internal energy and C_v is the specific heat in volume. During the phase change, the second term of (4.19) dominates [15], and the fluctuation of energy can be expressed as

$$\begin{aligned} \langle \delta E^2 \rangle &\approx kT \left(\frac{\partial U}{\partial N} \right)_{T,V} \left(\frac{\partial U}{\partial \mu} \right)_{T,V} \\ &\approx \left(\frac{\partial U}{\partial N} \right)^2_{T,V} \langle \delta N^2 \rangle. \\ \left(\frac{\partial U}{\partial N} \right)_{T,V} &= \mu - T \left(\frac{\partial \mu}{\partial T} \right)_{N,V}. \end{aligned} \tag{4.20}$$

The chemical potential of the semiconductor devices is the Fermi level energy. Since the Fermi level energy doesn't change significantly within temperature of interest (77K to 273K), the second term of eq (4.19) is negligible. Substituting eq (4.20) to eq (4.19) gives

$$\langle \delta E^2 \rangle = \mu^2 \langle \delta N^2 \rangle. \tag{4.21}$$

For our system (relaxation oscillator) specifically, the potential energy needed to add a charge on the top plate of capacitor is eV_{peak}. Thus, μ=eV_{peak}.

$$\langle \delta N^2 \rangle^{\frac{1}{2}} = \frac{1}{eV_{peak}} \langle \delta E^2 \rangle^{\frac{1}{2}}. \tag{4.22}$$

[3] Note that the following equation is, strictly speaking, developed under thermal equilibrium. Again, using the ergodic theorem, δE^2 is now interpreted ass statistical variance (obtained from time variance), and so is interpreted as the variance at thermal equilibrium.

4.3 Noise Fluctuation of Relaxation Oscillator at Classical Temperature Regime

When the temperature is high, $\beta \to 0$, by substituting (4.22) into (4.15), the fluctuation in term of normalized current can be calculated as

$$\begin{aligned}
\langle \delta N^2 \rangle^{\frac{1}{2}} &= \frac{1}{eV_{peak}} \left(V_{peak} \sqrt{\frac{kT \times RC_{gs}}{R(Rg_m - 1)}} \right). \\
\langle \delta I^2 \rangle^{\frac{1}{2}} &\propto \sqrt{\frac{kT}{R(Rg_m - 1)}}. \\
\frac{\langle \delta I^2 \rangle^{\frac{1}{2}}}{I_0} &\propto \frac{1}{\sqrt{g_m eV_{peak}}} \sqrt{\frac{kT}{R(Rg_m - 1)}} \\
&\propto \sqrt{\frac{kT}{eV_{peak}} \left(\frac{1}{g_m R(g_m R - 1)} \right)}.
\end{aligned} \tag{4.23}$$

The fluctuation of the normalized current obtained in (4.23) is not very different than (1.7) obtained from variable mapping with vdw gas[11], and (3.35) from section 3.4. Comparing (4.23) with (1.7)[11], it is found that when $g_m R \to 1$, (4.23), (1.7) and (3.35) are consistent. The difference of (4.23) and (1.7) is due to the fact that (1.7) is derived at metastable point only, while (4.23) is derived by taking account the trajectory of the neighbourhood of metastable point.In summary, comparison of present method with method 1, 2 tends to agree at high temperature or classical regime. This gives confidence to the present method, in particular when we generalize to low temperature or quantum regime.

4.4 Noise Fluctuation of Relaxation Oscillator at Low Temperature Regime

While (4.23) captures both the effects of thermal noise and the dynamic of the circuit, this fluctuation model is not complete because it is counter-intuitive to have the fluctuation goes to 0 when temperature, $T \to 0$. Thus, at low temperature, we substitute (4.22) into (4.18) and we have:

$$\frac{\langle \delta I^2 \rangle^{\frac{1}{2}}}{I_0} \propto \sqrt{\frac{\hbar \omega_0}{eV_{peak}} \left(\frac{1}{g_m R(g_m R - 1)} \right)}. \tag{4.24}$$

In this case, when temperature is low enough, $\hbar w_0$ dominates the noise source as shown in (4.24).

However, in the calculation of (4.24), the trajectory (with the corresponding equation of state) is assumed (in going from (4.15) to (4.16)) to stay much longer than around the metastable point (on the time scale of $\frac{1}{w_0}$). The resulting calculation of fluctuation becomes less accurate, as the actual trajectory (bounded by the regeneration time, t_{reg}) is less and less.

Essentially fluctuation is dictated by the time the circuit stays in metastable state (around the metastable point). This time, as T_{reg} decreases, is going to becomes less and less predicted by $\frac{1}{w_0}$. Therefore, (4.24) has to be refined, such that the effective $\hbar w_0$ is replaced. This becomes

$$\hbar w_0 \quad = \quad \hbar \times \frac{2\pi}{t_{reg}}. \tag{4.25}$$

t_{reg} in general depends on the overdrive voltage, current available and C_{gs}.To be more accurate it is obtained from the simulation. In the next section, we will discuss the microscopic aspect of this quantum fluctuation and shows its dependency on t_{reg}.

4.5 Explanation of Effective hw Qualitative Behaviour (microscopic) and How It Fits into kT fluctuation (microscopic)

The last section explains macroscopically (Langevin equation with one degree of freedom) the temperature behaviour. A microscopic discussion (with many degree of freedom), on the quantum aspect, is presented in this section. The background on quantum mechanics and density matrix is reviewed in Appendix F, following the treatment in [25]. We will do a qualitative description using an example.

4.5.1 hw Part(Arising from Time Evolution of State Ket of Pure State): 1 Single Electron Description

The ensemble is described by a Hamiltonian and the ensemble distribution. At $t < 0$, one of the transistor is on and the other transistor is off. The system is described by

Hamiltonian H_{stable}. At t=0, both the transistors are on and the system is described by $H_{metastable}$. Therefore, the eigenvalues and eigenkets change during the transition between transistors (M_1/M_2) on/off state to transistors (M_1/M_2) on/on state. At $0 < t < t_{reg}$, $H_{metastable}$ remains constant and $|a'\rangle$ is the eigenstates.[4].

We further assume that the ensemble distribution is at non-equilibrium, but remain constant during $0 < t < t_{reg}$. It only has significant change when $t > t_{reg}$, when eventually it settles to equilibrium, before one of the transistor turns off.

Let us start with the example of one electron, q_1 of the ensemble (lets say on top plate of capacitor C_{gs} of M_1, having state $|\alpha\rangle$. It is given as the superposition of energy eigenstates, so that $|\alpha\rangle = \sum c_{a'}|a'\rangle$. At t=0, $|\alpha, t = 0\rangle = \sum c_{a'}(0)|a'\rangle$. At some time later at t, the time evolution of state ket is $|\alpha, t\rangle = \sum c_{a'}(t)|a'\rangle$. Thus,

$$|\alpha, t\rangle = exp\left(\frac{-iE_{a'}t}{\hbar}\right)|\alpha, t = 0\rangle \tag{4.26}$$

$$= \sum |a'\rangle\langle a'|\alpha\rangle exp\left(\frac{-iE_{a'}t}{\hbar}\right). \tag{4.27}$$

i.e. $c_{a'}(t) = c_{a'}(0)exp\left(\frac{-iE_{a'}t}{\hbar}\right)$. An example of this is shown in Figure 4.1(a), where t=0, $c_1(0) = 0.71$, $c_2(0) = 0.55$, $c_3(0) = 0.32$, $c_4(0) = 0.32$...It then oscillates via $e^{\frac{-iE_{a'}t}{\hbar}}$ to $t = \frac{\hbar}{4E_1}$. i corresponds to energy eigenstate, E_i and weighting c_i. Next, we calculate the correlation, where in the special case, the initial ket $|\alpha\rangle$ is an eigenket of $H_{metastable}$, then this becomes

$$C(t) = \langle a'|a', t_0; t\rangle \tag{4.28}$$

$$= exp\left(\frac{-iE_{a'}t}{\hbar}\right). \tag{4.29}$$

With a continuum of eigenvalues this becomes, $c_{a'} \to g(E)|_{E=E_0}$ and:

$$C(t) = exp\left(\frac{-iE_0t}{\hbar}\right)\int dEg|\,(E)\,|^2\rho(E)exp\left(\frac{-i(E-E_0)t}{\hbar}\right) \tag{4.30}$$

with $\rho(E)$ characterizes the density of energy eigenstates. Then, $|g(E)|^2\rho(E)$ peaked around E_0 with width ΔE When t is large, the integrand of (4.30) over the many terms of

[4]Even though there is superposition of states, one can use the most probable energy to build our interaction energy(0.71=c_1 in Figure 4.1) to build our J model, as long as J is shown to depend on 'distance' (or equivalently one can use a weighed energy to calculate V_{peak}). Also, Pauli exclusion principle still works. Here quantum state, instead of eigenenergy, is a state that corresponds to a superposition.

oscillating time dependence of different frequencies cancel out and there is no contribution to C(t). However, when t is small, these oscillating terms don't cancel out. The characteristic time, t at which the correlation amplitude start appreciably cancel out the oscillating term is

$$t = \frac{\hbar}{\Delta E}. \tag{4.31}$$

This is describing the nature in which the state ket of q_1 starts to lose it character (less correlated) from the initial ket, as discussed above.

Meanwhile, looking at the expectation value of some observable B, when taken with respect to the basis of a superposition of energy eigenstates, then

$$\langle B\rangle = \sum\sum c_{a'} * c_{a"} \langle a'|B|a"\rangle exp\left(\frac{-i(E_{a"} - E_{a'})t}{\hbar}\right). \tag{4.32}$$

with $\Delta E = E_{a"} - E_{a'}$(=effective $\hbar w_0$). $\langle B\rangle$ oscillates with effective angular frequency, w_0. Next, take B to be the momentum operator of q_1, p. The fluctuation would allows us to measure fluctuation of the current density j since [26]:

$$j = tr(\hat{\rho}^{(1)}(t)\hat{j}(x)) \tag{4.33}$$

$$= \int d\alpha \int d\beta \rho^1_{\alpha\beta}(t) j_{\beta\alpha}(x) \tag{4.34}$$

where

$$j_{\beta\alpha}(x) = \frac{ie\hbar}{2M}\Psi_\beta * (x)\breve{D}\Psi_\alpha(x). \tag{4.35}$$

Here $\rho^1_{\alpha\beta}$ is the 1st order deviation, $\Psi_\beta(x)$ is the wavefuction in x representation for Hamiltonian having eigenstates indexed by variable α, β for electron wavefunction $|\alpha\rangle$. Then $j_{\beta\alpha}(x)$ are the matrix elements of the current density. In the present situation, where there is no magnetic field, the operator $\breve{D}$ =, is defined as ∇ the gradient or $\frac{i}{\hbar}p$, with p is the momentum operator. Then $\langle p\rangle$ oscillates with effective angular frequency w_0. Then, take a look at fluctuation [27] of p: $\Delta p = \langle(p - \langle p\rangle)^2\rangle^{\frac{1}{2}} = (\langle p^2\rangle - \langle p\rangle^2)^{\frac{1}{2}}$. Now since $\langle p\rangle$ oscillates with w_0, $\langle p^2\rangle$ also oscillates and therefore Δp oscillates. Pictorially from Figure 4.1, the components with higher eigenvalue oscillates more rapidly, and the contribution of these terms of higher frequencies to the correlation amplitude becomes less and less as time progresses. Then, the spread ΔE becomes narrower as shown in Figure 4.1 as t increases. In our case, t is simply t_{reg}, and with $\Delta E = \hbar w = \frac{2\pi\hbar}{t_{reg}}$ and this generates the fluctuation of i, Δi, we have equation (4.25).

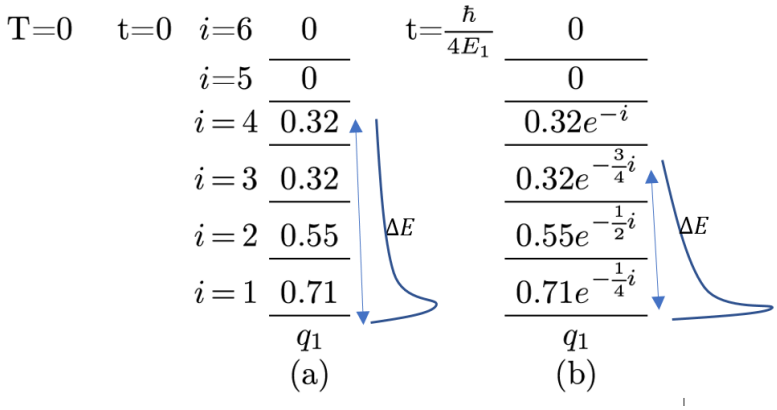

Figure 4.1: The time evolution of an electron , q_1 (in pure state).

4.5.2 hw Part(Arising from Time Evolution of Ensemble of Mixed State); Ensemble Evolution into Thermal Equilibrium and the kT part.

Looking at t=0, as shown in Figure 4.2(a), the trace of the density matrix of q_1 is 1, so each electron describes a pure state. Since the probability amplitudes, c's are different, the density matrix are different and thus the ensemble is a mixed ensemble. Referring to F.1, the weight of each of them is w_i ($w_1 = w_2$). As stated above, since the ensemble is at non-equilibrium, this weighting is not corresponding to Boltzmann distribution. Lets us assume $w_1 = w_2 = 0.5$, and it remains constant during $0 < t < t_{reg}$. The time evolution of the state ket $|\alpha_1\rangle$, $|\alpha_2\rangle$, is just like the case with one electron in Figure 4.1. Figure 4.2 shows the two kets dependency with time.

It should be noted that in general w_i changes with time. Given time, t longer than t_f, it later settles (via phonon scattering) into thermal equilibrium, and the ensemble of electrons settle into Fermi-Dirac distribution. For example, referring to Figure 3.3, when $T > 0$, the occupancy of electrons varies and this is characterized by the Fermi-Dirac distribution, with q_1 and q_2 being two of these electrons. The fluctuation is now kT in nature.

In summary, looking at the two temperature regime: at higher temperature regime, the t_{reg} is relatively larger than the scattering mean free time of the phonon [5] in the lattices of resistors. The overall noise is dominated by the thermal noise resulting from the

[5]The mean free path of electrons in n-type silicon is in the magnitude of 10^{-12} at room temperature

phonon scattering. When the temperature is lowered, the thermal agitation of the phonon is reduced and the mean free time is larger. It should be noted that t_{reg} is in the order of magnitude 10^{-13} from simulation shown in Appendix D and the mean free time is in the order of magnitude of 10^{-12} at room temperature. At some point, the regeneration time is smaller than the mean free time, and energy-time uncertainty relation contributes to the fluctuation of the system.

T=0 t=0

	q_1	q_2
i=6	0	0
i=5	0	0
i=4	0.32	0.32
i=3	0.32	0.45
i=2	0.55	0.71
i=1	0.71	0.45

(a)

$w_1 = 0.5 \quad w_2 = 0.5$

t=$\frac{\hbar}{4E_1}$

	q_1	q_2
	0	0
	0	0
	$0.32e^{-i}$	$0.32e^{-i}$
	$0.32e^{-\frac{3}{4}i}$	$0.45e^{-\frac{3}{4}i}$
	$0.55e^{-\frac{1}{2}i}$	$0.71e^{-\frac{1}{2}i}$
	$0.71e^{-\frac{1}{4}i}$	$0.45e^{-\frac{1}{4}i}$

(b)

$w_1 = 0.5 \quad w_2 = 0.5$

Figure 4.2: The time evolution of an ensemble with two electrons with $w_1 = w_2 = 0.5$.

Chapter 5

Experiment Results

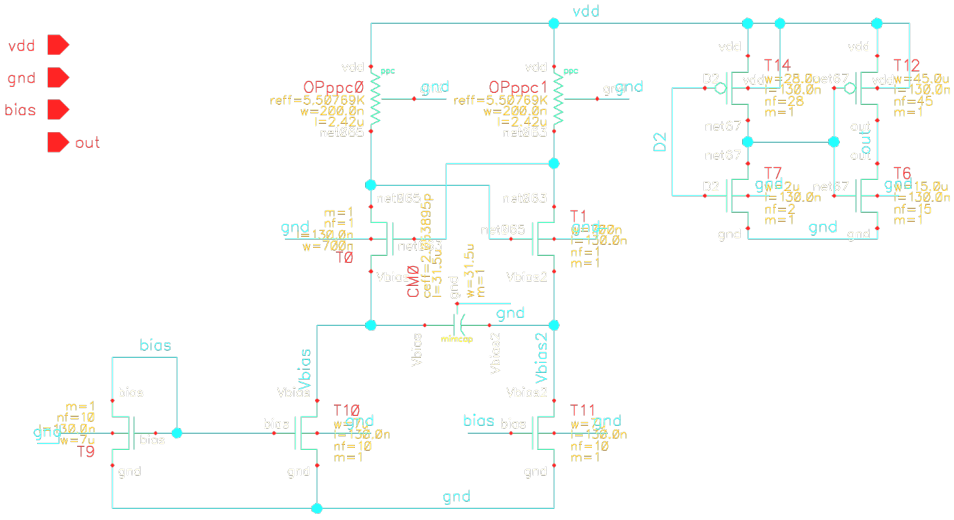

Figure 5.1: Schematic of Relaxation Oscillator.

Figure 1.3 is implemented in Cadence with 130nm CMOS technology and the schematic is shown in Figure 5.1. T9, T10, T11 are the transistors of the current mirror. The transistors T9, T10 and T11 are biased in saturation. The drain of transistor T9 is connected to a external potentiometer so that the current, I_0 in Figure 1.3 can be externally biased. T0 and T1 are the transistors for the cross coupled pair of the relaxation oscillator. The drain nodes of both transistors T0 and T1 are connected to resistors. T6, T7, T12, T14 are the output buffer of the relaxation oscillator. It consists of two inverters connected in

series. The switching threshold of the buffer is designed to be 0.6V. Four cases are implemented with different design parameters and are shown in Table 5.1. The chip layout is shown in Figure 5.2. The fabricated chip includes four relaxation oscillators with different design parameters and a Time-Digital Converter (TDC) which will be further elaborated in chapter 6.

		RO1	RO2
Current Mirror	$I_bias(uA)$	100	100
Transistors: T9, T10, T11	$W_n(\mu m)$	7	7
	$L_n(\mu m)$	0.13	0.13
Transistors: T0, T1	$W_n(\mu m)$	0.7	1.4
	$L_n(\mu m)$	0.13	0.13
Resistors: OPppc0, OPppc1	$R(k\Omega)$	5	5
Capacitor: CM0	$C(pF)$	2	2

Table 5.1: Design Parameters of Relaxation Oscillators

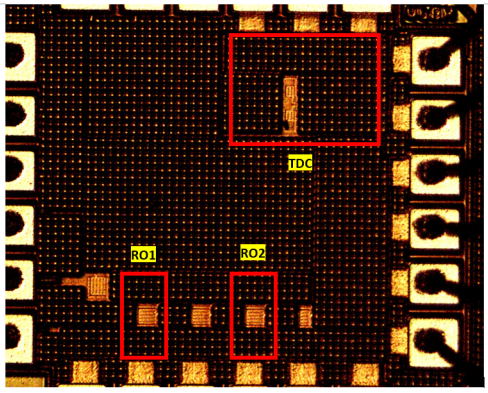

Figure 5.2: Fabricated Chip Microphotograph

A breakout PCB board is designed for the testing of the chips. A 10 $k\Omega$ potentiometer is chosen as the component used to bias the current, I_0 in the range from $80\mu A$ to $120\mu A$. A shunt is placed between the potentiometer and the pin of the chip (connected to the drain of the current mirror), so that the current can be externally measured. A 1μF capacitor parallel with a 0.1μF capacitor is connected from V_{DD} to ground to minimize the voltage ripples from the power supply. The output of the relaxation oscillators is connected to the SMA connectors. The schematic of the PCB breakout board is implemented using Eagle and is shown in Figure 5.3. The board layout is shown in Figure 5.4.

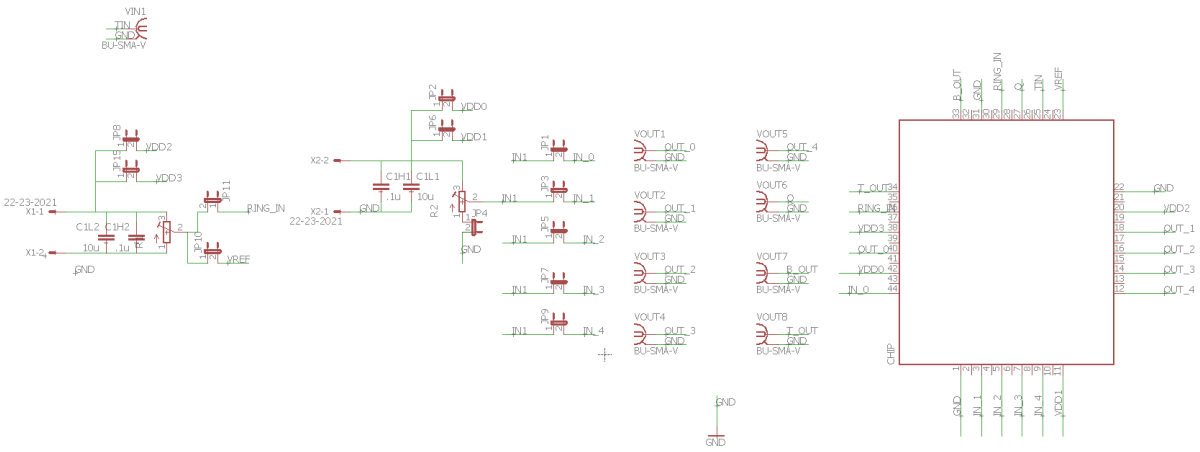

Figure 5.3: PCB Board Schematic

5.1 Functional Performance of Relaxation Oscillators

First, the functional simulation and measurement are performed. For supply voltage, V_{DD} set to 1.2V and the bias current set to $100\mu A$, the simulation performance of the relaxation oscillator, RO1 is shown in 5.5. The voltage net names of the signal are referenced to the the net names given in the schematic of relaxation oscillator shown in Figure 5.1. The functional measurement of RO1, with nominal V_{DD}=1.2V and current, I_0 biased at $100\mu A$, is shown in Figure 5.6.

The comparison between the oscillation frequencies of the relaxation oscillators (obtained from simulation and measurement) are shown in Table 5.2.

Relaxation Oscillators	Simulation Frequency (MHz)	Measurement Frequency (MHz)
RO1	48.65	41.11
RO2	33.41	27.0

Table 5.2: Oscillation Frequency of Relaxation Oscillators

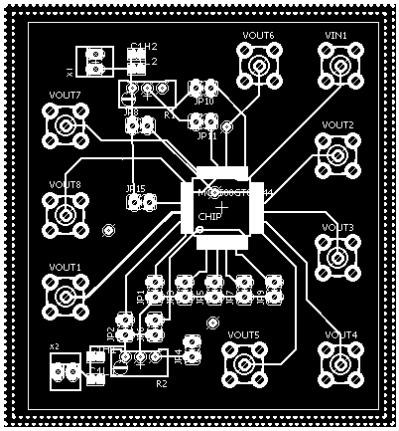

Figure 5.4: PCB Board Layout

5.2 The Phase Noise Measurements of Relaxation Oscillators

Next, the current fluctuation of the relaxation oscillator is measured when the temperature varies. The noise amplitude, $\frac{\langle \delta I^2 \rangle^{\frac{1}{2}}}{I_0} \propto \frac{\langle \delta V^2 \rangle^{\frac{1}{2}}}{V}$ and V is the V_{DD}. The time jitter value is a reflection of noise spike, $\langle \delta I^2 \rangle^{\frac{1}{2}}$ such that [1],

$$\langle \delta I^2 \rangle^{\frac{1}{2}} \quad \propto \quad \delta t \tag{5.1}$$

Therefore, phase noise at a fixed frequency is used as a metric of measurement to represent the time jitter, and thus, the noise spike. The devices under test are the relaxation oscillators, RO1 and RO2 with design parameters shown in Table 5.1. At room temperature, the measured oscillation frequency for RO1 (chip 1) and RO2 is shown in 5.2. The measured oscillation frequency for RO1 (chip 2) is 40.68MHz.

The setup of cryogenic experiment is shown in Appendix C. The controlled ambience temperature of the relaxation oscillators approximately ranges from 77K to 300K. For every temperature step, the phase noise of the relaxation oscillators are captured using Keysight N9010B EXA Signal Analyzer. To improve the accuracy of the measurement, the signal tracking feature of the Signal Analyzer is enabled to alleviate the effect of carrier frequency

[1] Time jitter is given as rms noise voltage divided by the slew rate of the timing waveform at triggering point. As the noise voltage increases, the time jitter increases as the slew rate stays relatively constant as shown in Appendix E.

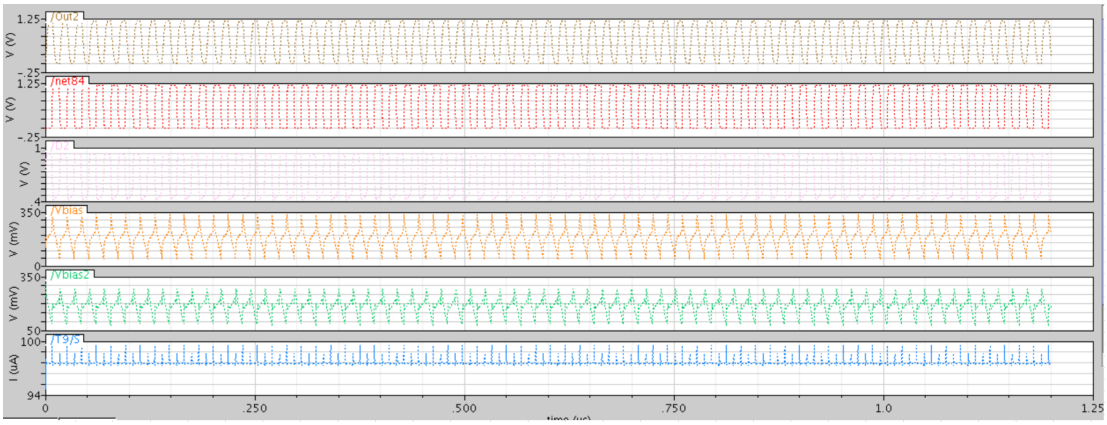

Figure 5.5: Functional Simulation Performance of Relaxation Oscillator, RO1

drift of the RO1. The phase noise of relaxation oscillators at the offset frequency 1MHz is used to indicate the degree of current fluctuation of the relaxation oscillators.

The phase noise log plots of RO1 (both chip 1 and chip 2) are obtained from the experiment. The offset frequency decade table for the phase noise of RO1 (chip 1) is shown in Figure 5.8. Trace 1 shows the raw trace and trace 2 displays the smoothed trace which averages a number of adjacent trace points from the raw trace. For consistency, the phase noise value is taken from trace 1. It is shown that the phase noise of RO1 (chip 1) with offset frequency 1MHz at temperature 77K is -82.81 dBc/Hz. Figure 5.9 shows the phase noise of RO1 at temperature 276.62K. The phase noise of RO1 with offset frequency 1MHz at temperature 276.62K is -79.51dBc/Hz.

The phase noise of RO1 (chip 1 and chip 2) with offset frequency 1MHz are summarized in Table 5.3 and Table 5.4 respectively.

It is shown from the Figure 5.10 that the phase noise of RO1 (chip 1) has two regions: In Region 1, the experiment data is proportional to $\sqrt{T}$ (in term of power, it is proportional to kT) as predicted by the phase noise model at high temperature limit, equation (4.23). In Region 2, the phase noise deviates from the $\sqrt{T}$ proportionality and becomes relatively constant. This trend agrees rather well with (4.24). The crossover temperature, T, depends on the value of effective quantum noise $\hbar w_0$, is approximately 120K.

With the same design parameters, the phase noise of RO1 (chip 1 and chip 2) is shown in Figure 5.11. The noise difference is due to process variation as both oscillates in slightly different frequencies. (Because of the process variation, RO1 chip 1 oscillates at 41.11MHz and RO2 chip 2 oscillates at 40.68MHz in room temperature)

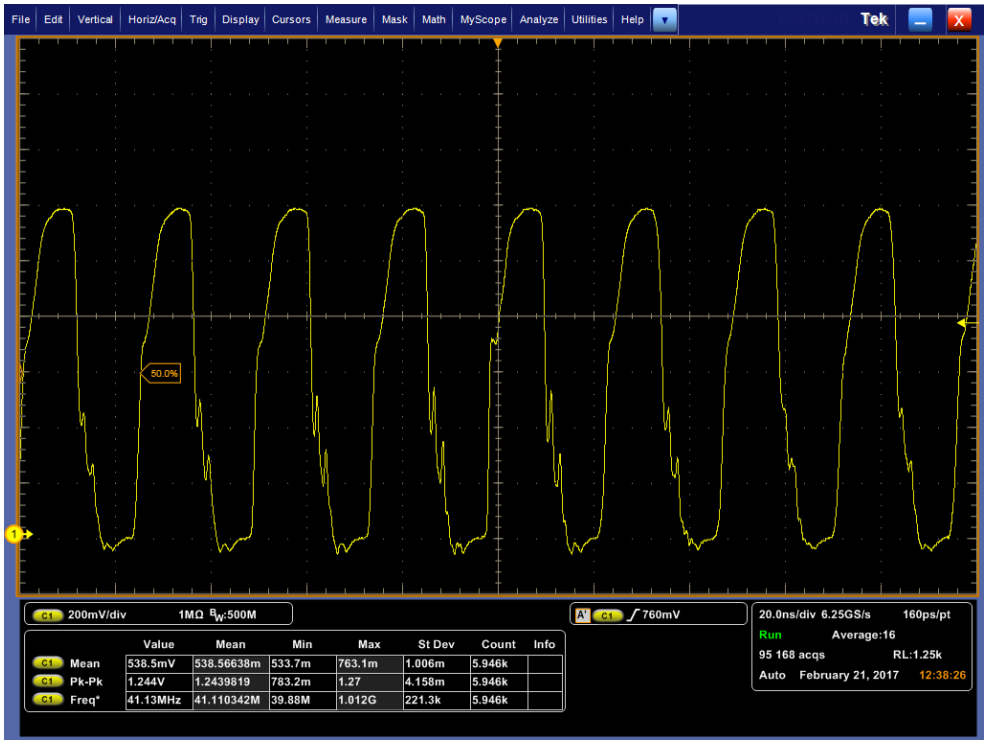

Figure 5.6: Functional Measurement Performance of Relaxation Oscillator, RO1

From simulation, the regeneration time, t_{reg} of RO1 is obtained to be 0.42ps for regeneration threshold voltage of 100mV around the metastable point as shown in Appendix D. From equation (4.24), this gives an effective $\hbar w_0$ and equating this to kT of equation (4.23), this gives the crossover temperature of 114K. This rather agrees with the experiment result where crossover temperature of 120K is obtained.

The aspect ratio of the transistor, $\frac{W}{L}$ of RO2 is twice the $\frac{W}{L}$ of RO1. Therefore, the gate-to-source capacitance, C_{gs} of RO2 is twice the C_{gs} of RO1. The RO2 extrapolated curve[2] in Figure 5.12. RO2 exhibits the two regions too as shown in Figure 5.10. As C_{gs} doubles, the overdrive voltage decreases by $\sqrt{2}$. Given that $t_{reg} = \frac{C_{gs}V_{ov}}{i_c}$ (i_c is the current flowing through the capacitance, it is assumed to be constant), the regeneration time is

[2] g_mR of RO2 is biased at 1.56. Theoretically, g_mR of RO2 can be set to 1.1 with I_0 reduced by half. However, this would cause the output dc voltage of relaxation oscillator to increase. The relaxation oscillator is followed by a buffer circuit with switching threshold voltage of 0.6V. By increasing the output dc voltage of relaxation oscillator, the output signal after the buffer stops to oscillate. Because of this, extrapolation of RO2 curve at $g_mR = 1.1$ is presented

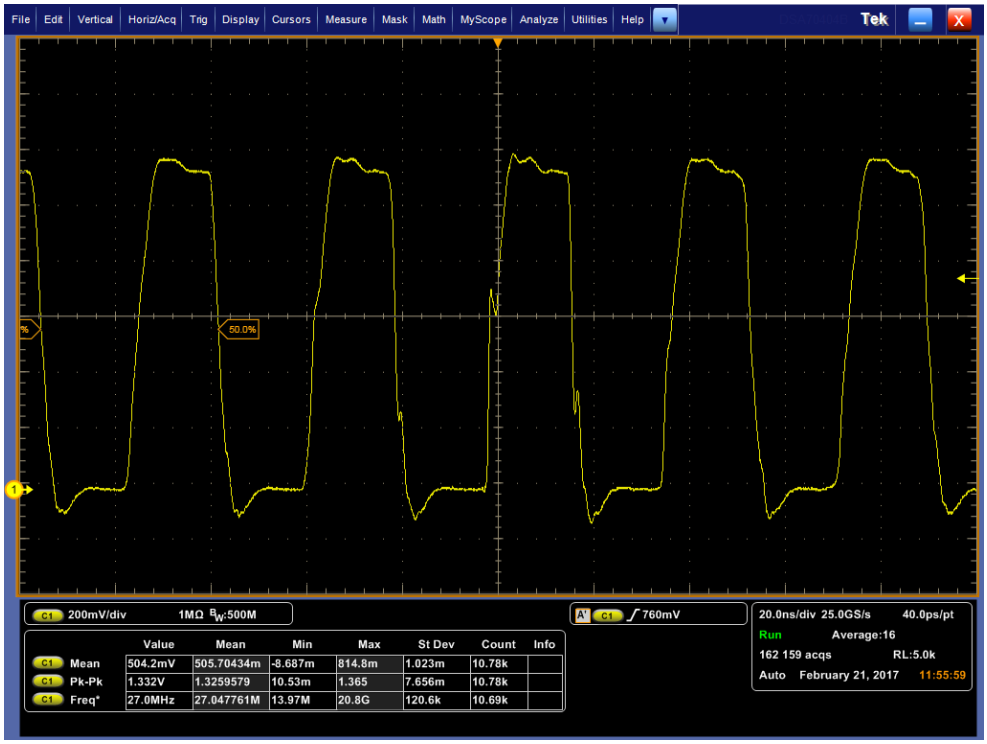

Figure 5.7: Functional Measurement Performance of Relaxation Oscillator, RO2

increased by $\sqrt{2}$. So,the effective w_0 is reduced by $\sqrt{2}$ and therefore, crossover temperature is reduced by $\sqrt{2}$. By the crude estimation, the crossover temperature for RO2 is 80.6K. The measured crossover temperature for RO2 is around 100K.

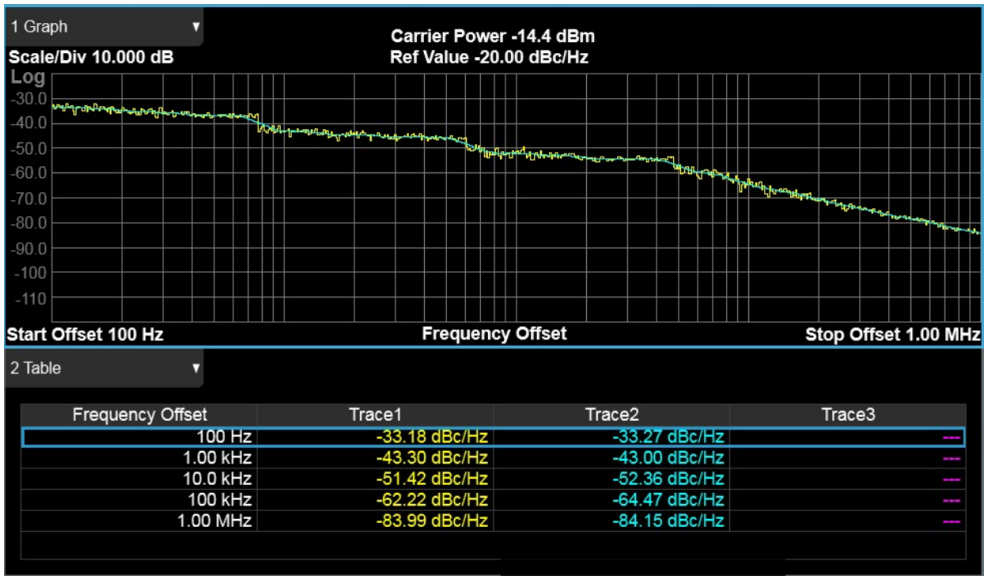

Figure 5.8: Phase Noise Measurement of RO1 at 77K

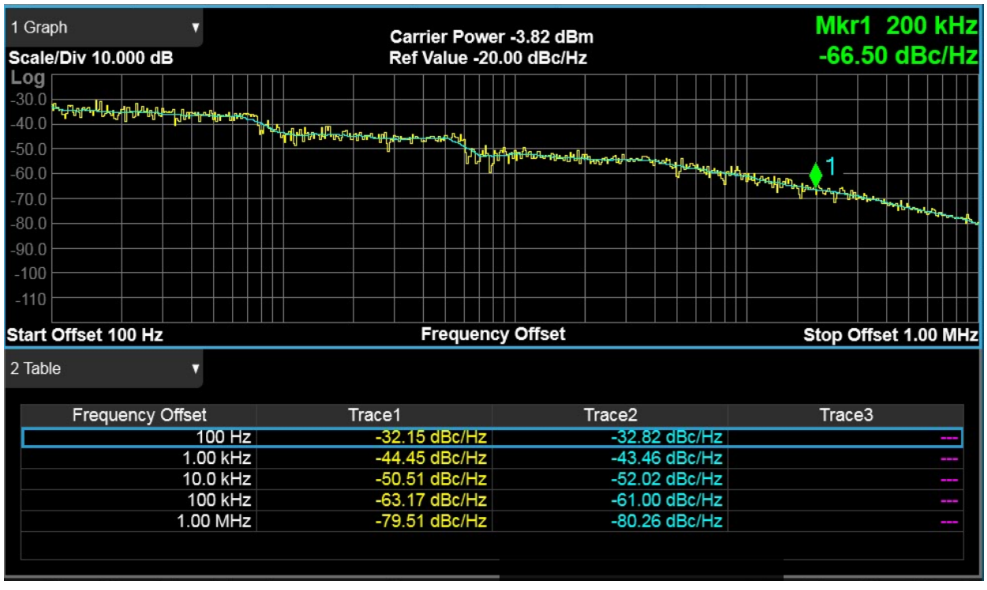

Figure 5.9: Phase Noise Measurement of RO1 at 276.62K

Temperature (K)	RO1 (chip 1) Experimental Phase Noise (dBc/Hz)
77.00	-83.99
81.00	-83.38
106.71	-83.02
113.17	-83.12
120.00	-83.40
121.22	-83.76
143.53	-81.89
153.89	-82.53
158.34	-81.68
174.00	-81.74
178.82	-81.14
202.04	-80.61
228.3	-80.37
262.74	-79.76
276.62	-79.51

Table 5.3: Experiment Results of RO1 (chip 1)

Temperature (K)	RO1 (chip 1) Experimental Phase Noise (dBc/Hz)
77.66	-84.04
82.00	-84.16
88.00	-83.94
106.98	-84.44
116.00	-84.61
126.78	-83.99
144.28	-83.57
166.76	-83.04
184.00	-82.32
209.00	-81.95
224.00	-81.65
248.00	-81.29
265.22	-80.35
271.00	-79.85

Table 5.4: Experiment Results of RO1 (chip 2)

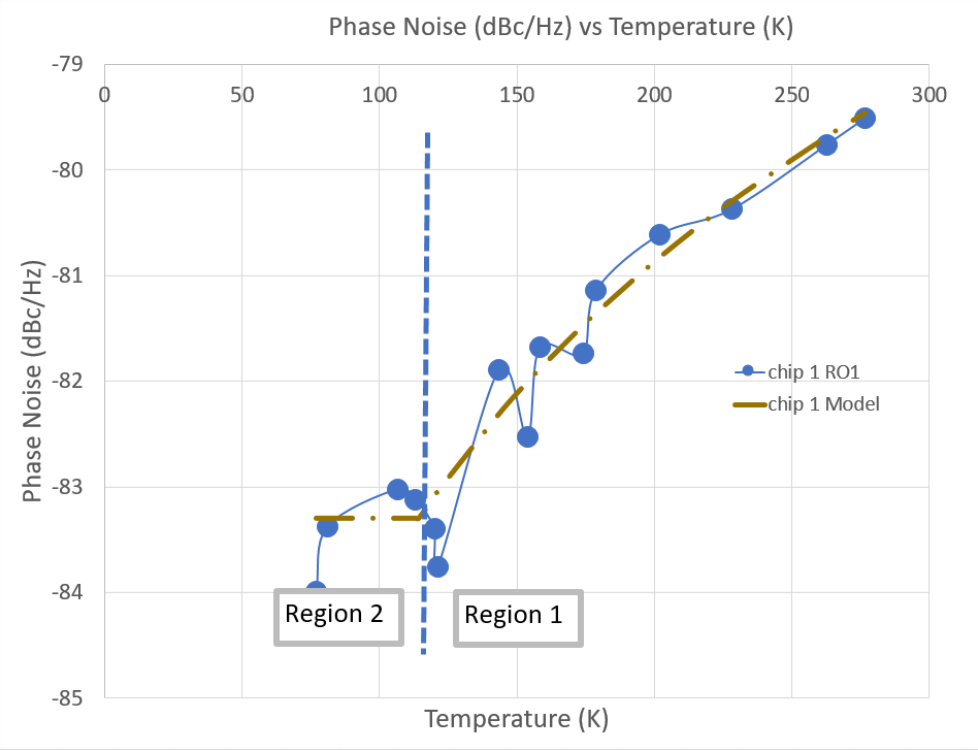

Figure 5.10: Comparison between experiment data of relaxation oscillator, RO1 with the phase noise model at high temperature limit. RO1 is biased at $g_m R = 1.1$. The model curves of RO1 is the fitting curves of equation (4.23). In Region 1, the experiment data agrees well with the trend of fitting curves of phase noise model at high temperature limit. In Region 2, the experiment data agrees well with the trend of phase noise model at low temperature, equation and it is relatively constant.

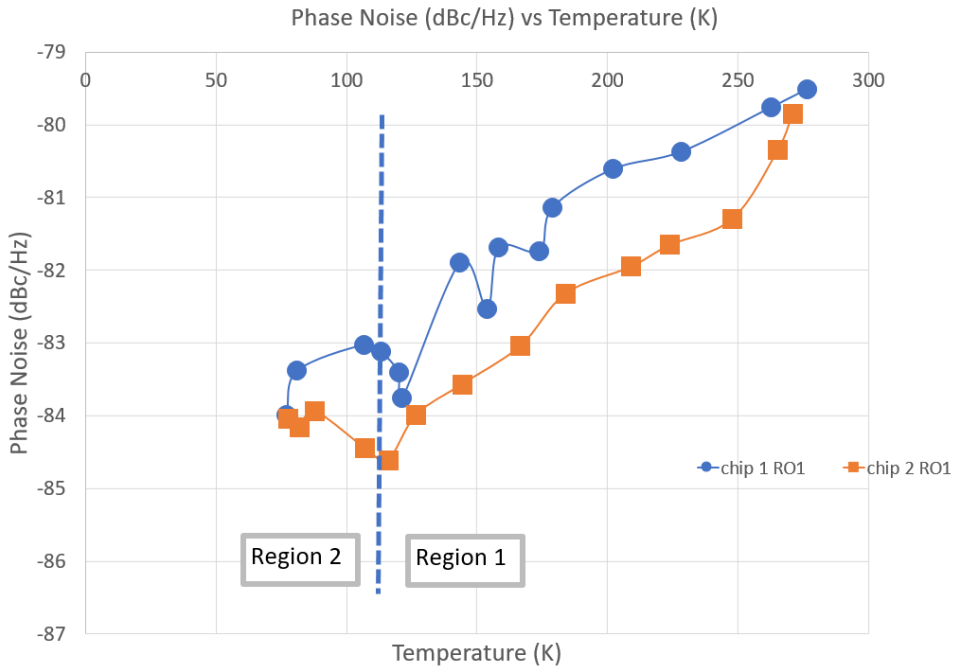

Figure 5.11: Comparison between experiment data of relaxation oscillators, RO1 (chip 1 and chip 2)

Temperature (K)	RO2 Experimental Phase Noise (dBc/Hz)
77.00	-95.27
85.00	-95.02
108.09	-95.30
123.60	-94.62
132.00	-93.75
141.22	-93.36
161.54	-92.48
191.50	-92.19
215.23	-91.36
225.06	-91.5
261.20	-90.54
274.33	-90.62

Table 5.5: Experiment Results of RO2

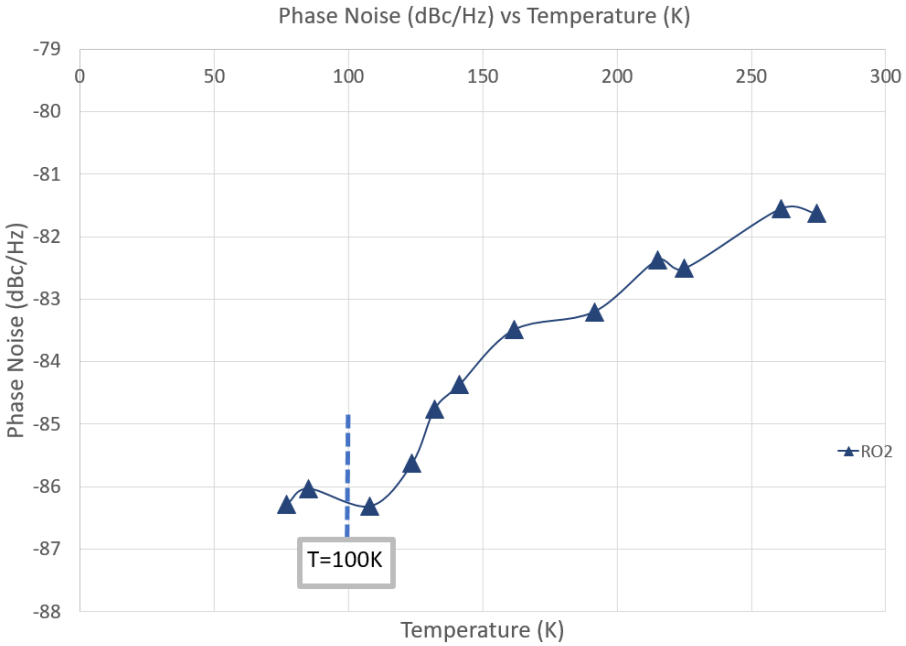

Figure 5.12: The experiment data of relaxation oscillators, RO2

Chapter 6

Application of Relaxation Oscillator in Time to Digital Converter

In this chapter, an example of application for relaxation oscillator is presented.The relaxation oscillator can be implemented in the first order noise-shaping Time-to-digital converter (TDC) circuit. TDC has been gaining popularity as an alternative of Analog-to-digital converter (ADC) in low power technologies. In particular, the representation of signal in time domain has the advantages from the continuous scaling of CMOS technology. Scaling in deep sub-micron regime gives the advantage of fast switching speed, and this improves the temporal resolution. In contrary, the amplitude resolution does not have a good scaling behavior with technology. This is because, in the voltage domain, V_{DD} is lowered from technology scaling, resulting the voltage swing of the signal in voltage domain representation is reduced. Since the noise doesn't scale, the signal to noise ratio (SNR) is reduced from the smaller voltage swing. Given the advantages of TDC with scaling, the discussion of an error-feedback structure TDC, with relaxation oscillator for clock generation of sampling signal, is given. In this case, the present noise model (with noise spikes included) becomes important in predicting and minimizing the noise for low power TDC.

The goal of the design is to obtain the required resolution for TDC with low power budget. There is a design trade off among resolution, signal-to-noise ratio (SNR) and power for TDC. In $\Sigma\Delta$ TDCs, the raw resolution (the minimum quantization step; in this case, the period of the relaxation oscillator, T_{OSC}) can be improved with oversampling and noise shaping.The noise free effective resolution for a first order noise shaping TDC is

$$T_{eff} = \frac{\pi T_d}{6 \times OSR^{\frac{3}{2}}}. \tag{6.1}$$

with T_d is the raw resolution and OSR is the oversampling ratio. OSR is defined to be

$$OSR = \frac{f_s}{2f_0}. \tag{6.2}$$

where $f_s$is the sampling frequency, and f_0 is the signal bandwidth. By including the noise from the circuit, the achievable resolution will be worse. The finest achievable resolution is practically limited by the jitter noise of the relaxation oscillator. Thus, understanding the nature of noise of relaxation oscillator becomes important.

With the increase of OSR, the resolution becomes smaller. Since the quantization noise power is proportional to resolution of TDC, the quantization noise power is reduced. Subsequently, the SNR of the TDC is improved. To increase the OSR, the sampling frequency (the oscillation frequency of relaxation oscillator) of the TDC can be maximized. This can be done by having the design parameters of relaxation oscillator, $g_m R \to 1$ while the power consumption of the relaxation oscillator remains the same (bias current remains the same). The trade-off for the increase of sampling frequency is the manifestation of noise spike due to regeneration. The noise model presented becomes important for the design strategy to obtain the optimal SNR, where the total noise of both quantization noise and the regeneration noise spike is minimal.

Referencing to [6], the TDC is designed and fabricated using 130nm CMOS technology in Cadence. The block diagram of the TDC is shown in Figure 6.1.

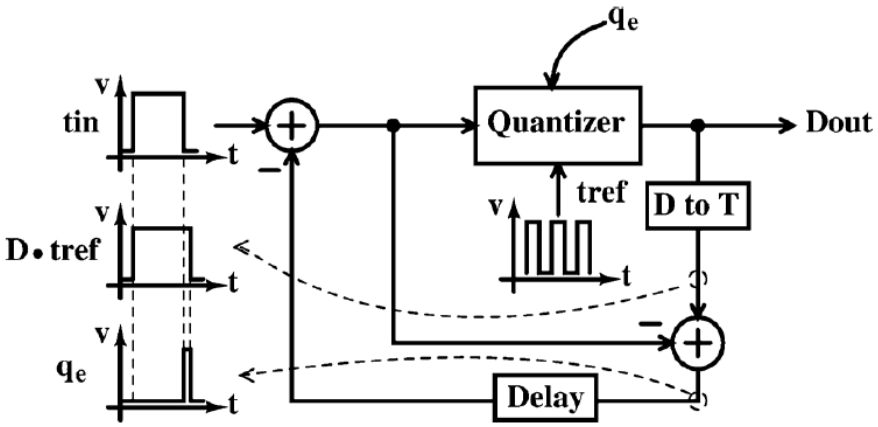

Figure 6.1: The Block Diagram of relaxation oscillator based TDC [6]

The schematic of the TDC is shown in Figure G.1. The design parameters of the TDC is given in Appendix G. This TDC consists of SR-flip flop and comparator-type

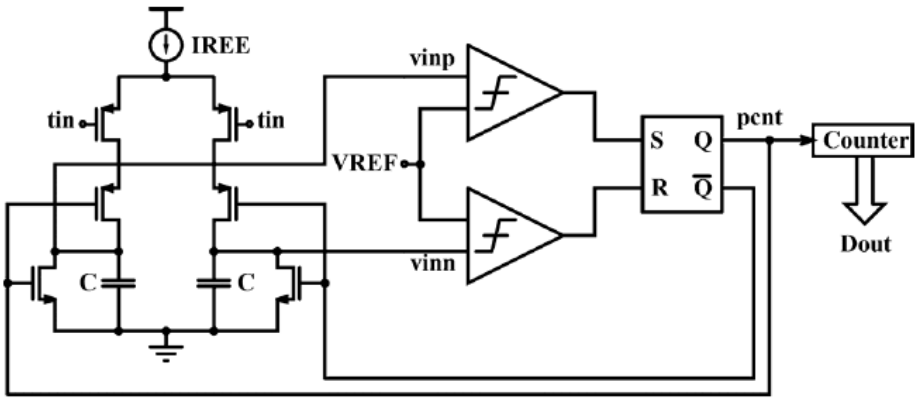

Figure 6.2: The schematic of relaxation oscillator based TDC [6]

RC relaxation oscillator. The schematic of the comparator is shown in Figure G.2. This threshold detection comparator consists of four stages, with the first three stages consume $120\mu A$ and the last stage consumes $240\mu A$. The single-ended output signals (V_{inp} and V_{inn}) from the relaxation oscillator are compared with the external reference voltage, V_{ref} with two comparators, I0 and I3. The outputs of the comparators are connected to a SR flip-flop. The design parameters of the comparator is summarized in Table G.2. The schematic of the SR flip-flop is shown in Figure G.3. The design parameters of the SR flip-flop is shown in Table G.3.

The TDC is based on the error-feedback structure. The operation of the TDC is as following: First, the input signal, t_{in} is sampled using the reference clock, t_{ref}. The sampled output is fed to an external counter which is the quantizer of the TDC circuit. When the input signal, t_{in} is low, the oscillation at the output signal stops. The quantization error is stored on the capacitor in the relaxation oscillator as residue voltage. The stored quantization error is then added to the next cycle of t_{in} when the oscillation starts again. Since the quantization error is fed back to the input, a first order noise shaping is obtained. The simulation of the TDC with a square wave signal input, as shown in Figure 6.3, shows the residue voltage (quantization error) of the capacitor is stored and transferred to the next cycle of oscillation. The sampling frequency from the simulation is 54.98MHz. From the simulation, the power consumption for the entire TDC is approximately 2.06mW [1].

The measured functional operation of the fabricated TDC is presented in this work.

[1]The power consumption of the comparators can further be optimized by enabling the comparator only when its connected capacitor is being charged [6]

From Figure 6.4, the sampling frequency from the measurement is 48.4MHz. The output waveform of TDC operation with 5kHz square wave input is shown in Figure 6.4. The measurement has the same waveform as the simulation.

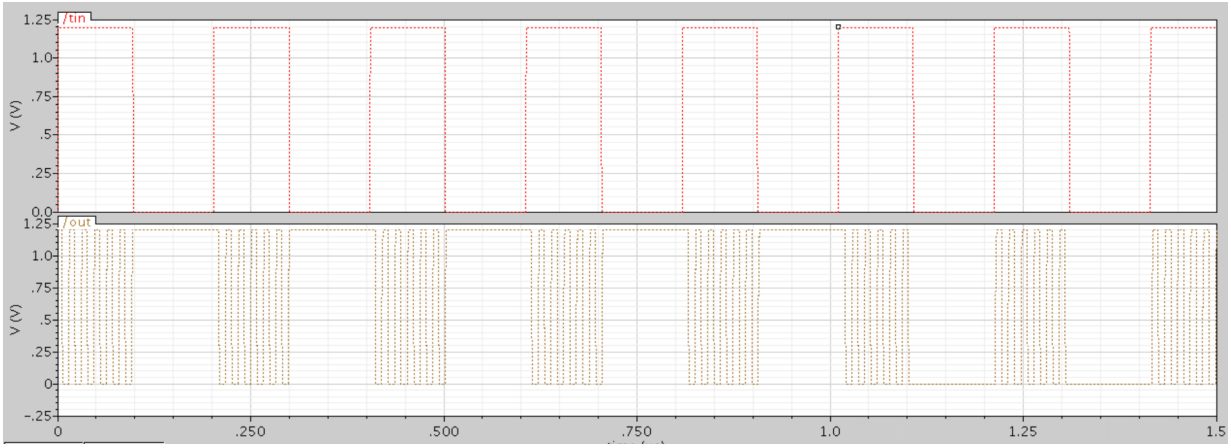

Figure 6.3: Simulation waveform for TDC with T_{in}=10T_{ref}. Referring to the block diagram, Figure 6.1, q_e=0

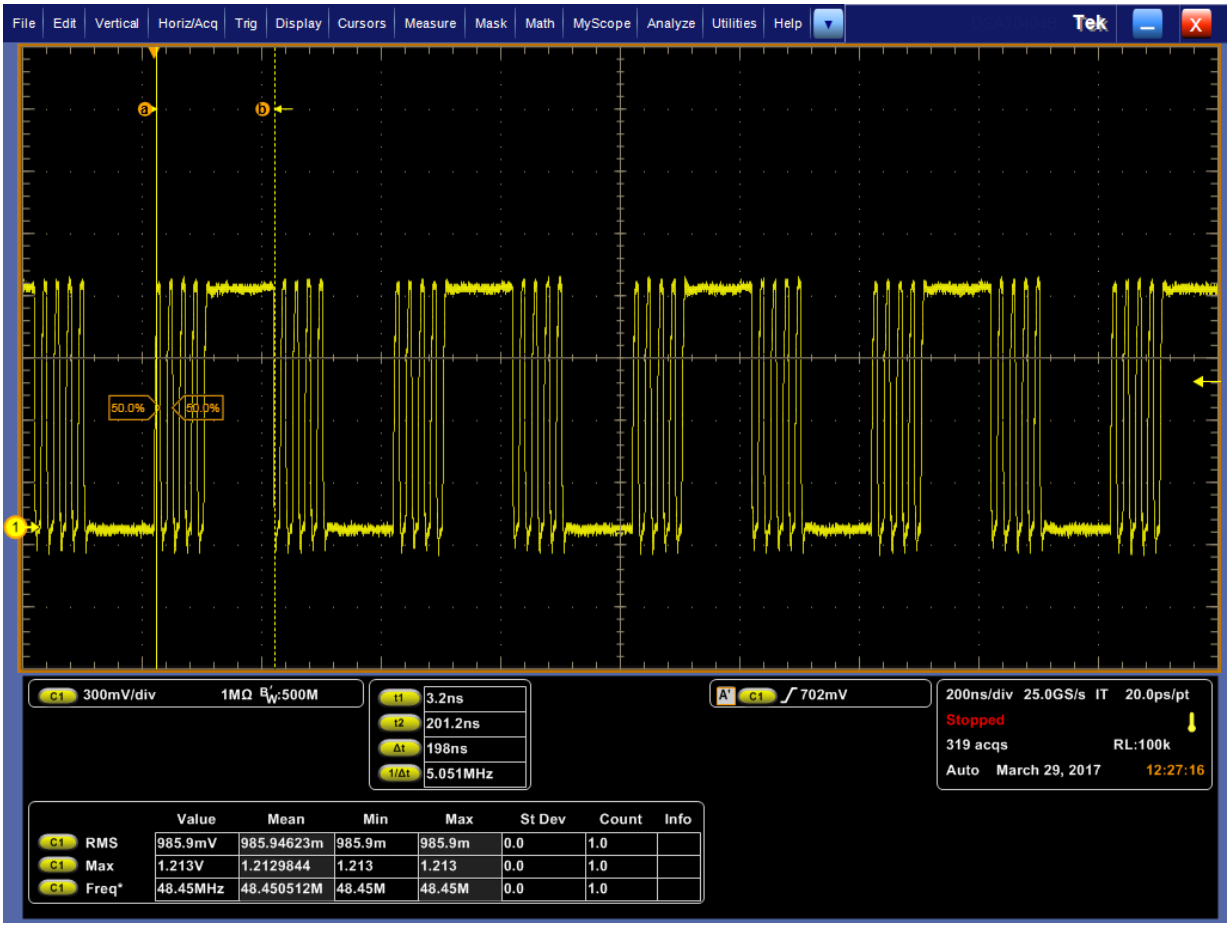

Figure 6.4: Measured functional waveform for TDC with T_{in}=10T_{ref}. Referring to the block diagram, Figure 6.1, q_e=0

Chapter 7

Conclusions

The noise spike model of relaxation oscillator with design parameter loop gain $\rightarrow 1$ is investigated as temperature varies (cryogenic range down to 77K), for possible application in Time-to-Digital Converter (TDC) design in quantum computing. In Chapter 2, *Method 1* is performed with the underlying assumption that the system can be represented by one degree of freedom. The physical interpretation of the potential energy is given to be of the electrostatic potential differential energy between the gate-to-source capacitors in transistors, C_{gs1} and C_{gs2}. The system consists of the electrons on the top plates of C_{gs1} and C_{gs2}, whereas these electrons travel through the resistors and experience the interaction energy from the cross-coupled topology of the transistors. It is shown that the metastable state has the highest potential energy, and through regeneration, will have the energy lowered to the lowest potential energy and settle to a stable state. It is found that the potential energy with this nature is due to the symmetrical cross-coupling of the electronic circuit, thus relating the potential energy with the design parameters of the electronic circuit. The limitation of *Method 1* is that it ignores the many internal degree of freedom (i.e. the charges distribution over energy levels in phase space/eigenenergies), which is important as temperature changes.

This limitation is overcome in Chapter 3 by investigating the different configuration in which these internal degrees of freedom manifest (*Method 2*). The free energy obtained shows the dependency of temperature in the equation. From the free energy, the noise model is obtained and it is consistent with the existing noise model in [11], but with more insights on the thermodynamic quantities. However, when the temperature goes down enough, *Method 2* (i.e. classical) becomes invalid as the quantum noise might manifest.

An alternative, *Method 3*, is presented in Chapter 4. The system is represented by one

degree of freedom but with the internal degree of freedom decoupled and assumed to be represented by the immersion of the system in a heat bath with many degrees of freedom. The manifestation of the quantum noise, $\hbar w_0$ is obtained in the phase noise model in the low temperature limit, with w_0 characterizes the regeneration time of relaxation oscillator.

The experimental results, presented in Chapter 5 show the phase noise of the relaxation oscillator has two regions: at higher temperature, the phase noise is consistent with the noise model where the phase is proportional to $\sqrt{T}$; at lower temperature, the phase noise becomes relatively constant. The crossover temperature between these both regions is investigated. With the design parameter of the relaxation oscillator varies, the crossover temperature shifts as predicted by the noise model.

In Chapter 6, the measured functional operation of the fabricated 1-bit $\Sigma\Delta$ TDC and it operates at 48.4MHz, agreeing with simulation. The phase noise model can be applied in such application.

The key contributions of this thesis can be summarized as below:

1. Provide noise model for both high-temperature limit (thermal noise) and low temperature limit (quantum noise) of relaxation oscillator in cryogenic range (77K to 273K)

2. Noise model is verified by experiment results. Two temperature trends is observed as predicted by the noise model.

References

[1] Harald Homulle, Stefan Visser, and Edoardo Charbon. A cryogenic 1 gsa/s, soft-core fpga ADC for quantum computing applications. *IEEE Transactions on Circuits & Systems I Regular Papers*, 63(11):1854–1865, 2016.

[2] J. Mavor. *Bipolar and MOS Analog Integrated Circuit Design*. J. Wiley, 1984.

[3] Zhentao Xu, Wei Wang, Ning Ning, and Meng Lim Wei. A supply voltage and temperature variation-tolerant relaxation oscillator for biomedical systems based on dynamic threshold and switched resistors. *IEEE Transactions on Very Large Scale Integration Systems*, 23(4):786–790, 2015.

[4] Huan Hu, Subhanshu Gupta, and Martin Schiavenato. An 143nw relaxation oscillator for ultra-low power biomedical systems. *2016 IEEE Conferences: Sensor*, pages 1–3, 2016.

[5] Hyunwoo Cho, Hyunki Kim, Minseo Kim, Jaeeun Jang, Yongsu Lee, Kyuho Jason Lee, Joonsung Bae, and Hoi Jun Yoo. A 79 pj/b 80 mb/s full-duplex transceiver and a 42.5 μW 100 kb/s super-regenerative transceiver for body channel communication. *IEEE Journal of Solid-State Circuits*, 51(1):310–317, 2016.

[6] Y Cao, W De Cock, M Steyaert, and P Leroux. 1-1-1 mash time-to-digital converters with 6 ps resolution and third-order noise-shaping. *Solid-State Circuits, IEEE Journal of*, 47(9):2093–2106, 2012.

[7] H. Asano, T Miyoshi, K Tsubaki, T Ozaki, N. Kuroki, and M. Numa. A fully integrated, 1-s start-up time, 32-mhz relaxation oscillator for low-power intermittent systems. *2016 14th IEEE International New Circuits and Systems Conference (NEWCAS)*, pages 1–4, 2016.

[8] B Razavi. A study of phase noise in cmos oscillators. *IEEE Journal of Solid-State Circuits*, 31(3):331–343, 1996.

[9] A. A. Abidi and R. G. Meyer. Noise in relaxation oscillators. *IEEE Journal of Solid-State Circuits*, 18(6):794–802, 1983.

[10] A. Buonomo and A. Lo Schiavo. Analysis of emitter (source)-coupled multivibrators. *Circuits & Systems I Regular Papers IEEE Transactions on*, 53(6):1193–1202, 2006.

[11] Bosco H. Leung. Noise spike model in relaxation oscillators based on physical phase change. *IEEE Transactions on Circuits & Systems I Regular Papers*, 63(6):871–882, 2016.

[12] S. S Sastry. The effects of small noise on implicitly defined nonlinear dynamical systems. *IEEE Transactions on Circuits & Systems*, 30(9):651–663, 1982.

[13] Radit Smunyahirun and Eng Leong Tan. Derivation of the most energy-efficient source functions by using calculus of variations. *IEEE Transactions on Circuits & Systems I Regular Papers*, 63(4):494–502, 2016.

[14] Adel S. Sedra and Kenneth C. Smith. Microelectronic circuits. 2010.

[15] R. K. Pathria. *Statistical Mechanics (Second Edition)*. 1996.

[16] A Hajimiri and T. H Lee. A general theory of phase noise in electrical oscillators. In *IEEE J. Solid-State Circuits*, pages 179–194, 1998.

[17] S.H. Strogatz. *Nonlinear Dynamics and Chaos: With Applications to Physics, Biology, Chemistry, and Engineering*. Advanced book program. Westview Press, 1994.

[18] Ying Cao, P Leroux, W De Cock, and M Steyaert. A 63,000 q-factor relaxation oscillator with switched-capacitor integrated error feedback. In *Solid-State Circuits Conference Digest of Technical Papers*, pages 186–187, 2013.

[19] S Hashemi and B Razavi. Analysis of metastability in pipelined ADCs. *IEEE Journal of Solid-State Circuits*, 49(49):1198–1209, 2014.

[20] P. M Figueiredo. Comparator metastability in the presence of noise. *Circuits & Systems I Regular Papers IEEE Transactions on*, 60(60):1286–1299, 2013.

[21] Pierluigi Nuzzo, Fernando De Bernardinis, Pierangelo Terreni, and Geert Van Der Plas. Noise analysis of regenerative comparators for reconfigurable ADC architectures. *IEEE Transactions on Circuits & Systems I Regular Papers*, 55(6):1441–1454, 2008.

[22] Sanu K. Mathew, David Johnston, Sudhir Satpathy, and Vikram Suresh. RNG: A 300950 mv, 323 gbps/w all-digital full-entropy true random number generator in 14 nm finfet cmos. *IEEE Journal of Solid-State Circuits*, 51(7):1695–1704, 2016.

[23] C. E Smith. Lagrangians and Hamiltonians with friction. *Journal of Physics Conference Series*, pages 1303–1347, 2010.

[24] David Chandler. *Introduction to Modern Statistical Mechanics*. Oxford University Press, 1987.

[25] J. J. Sakurai, S. F. Tuan, and Eugene D. Commins. Modern quantum mechanics, revised edition. 1995.

[26] Thomas Dittrich, Peter Hnggi, Gert Ludwig Ingold, Bernhard Kramer, Gerd Schn, and Wilhelm Zwerger. *Quantum transport and dissipation*. Wiley-VCH, 1998.

[27] Ramamurti Shankar. *Principles of quantum mechanics 2nd Edition*. Plenum Press, 1988.

[28] Y. C. Chen, Matthew P. A. Fisher, and A. J. Leggett. The return of a hysteretic Josephson junction to the zero voltage state: iv characteristic and quantum retrapping. *Journal of Applied Physics*, 64(6):3119–3142, 1988.

[29] Antonio Barone and Gianfranco Patern. *Physics and Applications of the Josephson Effect*. Wiley-Interscience Publication, 1982.

[30] Pavel L Krapivsky, Sidney Redner, and Eli Bennaim. *Kinetic view on statistical physics*. Cambridge University Press, 2013.

[31] R. J. Mccraw and L. S. Schulman. Metastability in the two-dimensional ising model. *Journal of Statistical Physics*, 18(3):293–308, 1978.

APPENDICES

Appendix A

Simulation Syntax

A.1 Eldo Simulation Codes for Noise Spikes in Relaxation Oscillator

```
.lib '/home/yc2ng/Documents/ECE444/Simulation/rf018.eldo' TT
.subckt multi_vib D1 G1

M1 D1 G1 S1 B1 nch w=0.65u l=0.13u
M2 G1 D1 S2 B2 nch w=0.65u l=0.13u

R1 D1 SUPPLY 5k
R2 G1 SUPPLY 5k
I1 S1 0 110e-6
I2 S2 0 110e-6
C1 S1 S2 1p
V1 SUPPLY 0 1.2V
VB1 B1 0 0
VB2 B2 0 0

.ends multi_vib

X1 OUT1 OUT2 multi_vib

.NOISETRAN FMIN=10000 FMAX=500MEG NBRUN=10 MRUN
```

```
.tran 2p 500n
.plot tran V(OUT1) V(OUT2)
.op
.ic v(OUT1) 0.9v
.ic v(OUT2) 1.1v
.extract tran gm(X1.M1)
.extract tran cgs(X1.M1)
.extract tran cgd(X1.M1)
.plot tsst v(OUT1, OUT2)
.end
```

A.2 Mathematica Codes for Bistable Circuit

The Mathematica codes for the phase portrait of normalized current as shown in Figure 2.2:

```
vt=0.4; I0=1;R=0.9; kn=2;
splot=StreamPlot[{\[Sqrt](2*kn*x)*(I0/2+1/(2*R)*(\[Sqrt](2*y/kn)-
\[Sqrt](2*x/kn))-y),\[Sqrt](2*kn*x)*(I0/2-1/(2*R)*(\[Sqrt](2*y/kn)-
\[Sqrt](2*x/kn))-x)},{x,0,1},{y,0,1},StreamColorFunction->"Rainbow"];
Show[splot, Frame->True, FrameLabel->{"Subscript[i, d1]/Subscript[I, 0], A",
"Subscript[i, d2]/Subscript[I, 0], A"}, BaseStyle->{FontSize-> 14}]
```

The Mathematica codes for the time evolution of the normalized current as shown in Figure 2.4:

```
sol=NDSolve[{x'[t]==\[Sqrt](2*x[t]*kn)*(I0/2+1/(2*R)*(\[Sqrt](2*y[t]/kn)-
\[Sqrt](2*x[t]/kn))-y[t]),y'[t]==\[Sqrt](2*y[t]*kn)*(I0/2-1/(2*R)*
(\[Sqrt](2*y[t]/kn)-\[Sqrt](2*x[t]/kn))-x[t]),x[0]==0.5, y[0]==0.51},
{x,y},{t,50}];
Plot[Evaluate[{x[t],y[t]}/.sol],{t,0, 50},PlotRange->All,AxesOrigin->{0, -0.1},
AxesLabel->{"Time(s)", "Current (A)"}, PlotStyle->{Dashed, Thick},
PlotLabels->{"Subscript[i, d1]/Subscript[I, 0]",
"Subscript[i, d2]/Subscript[I, 0]"}]
```

The Mathematica codes for the Phase curve of normalized current as shown in Figure 2.3:

```
sol=NDSolve[{x'[t]==\[Sqrt](2*x[t]*kn)*(I0/2+1/(2*R)*(\[Sqrt](2*y[t]/kn)-
\[Sqrt](2*x[t]/kn))-y[t]),y'[t]==\[Sqrt](2*y[t]*kn)*(I0/2-1/(2*R)*
(\[Sqrt](2*y[t]/kn)-\[Sqrt](2*x[t]/kn))-x[t]),x[0]==0.5, y[0]==0.51},
{x,y},{t,50}];
ParametricPlot[Evaluate[{(x[t]),y[t]}/.sol],{t,0,50},PlotRange->{0,1},
Frame->True,FrameLabel->{"Subscript[i, d1]/Subscript[I, 0], A",
"Subscript[i, d2]/Subscript[I, 0], A"}, BaseStyle->{FontSize-> 14},
PlotStyle->{Red, Thickness[0.02]}, GridLines->Automatic
```

Appendix B

Fast Dynamic and Slow Dynamic of Relaxation Process

The whole cycle of oscillation of relaxation oscillator can be separated into a regeneration (fast) phase, and a charging/discharging (slow) phase. An attempt to connect the modelling the relaxation oscillator as a bistable circuit/charging-discharging timing capacitor C combination, to modelling of the relaxation oscillator as a circuit having time scale separation (slow-fast dynamics), was given below.

The circuit 1.5 with parasitic capacitance C_{gs1} and C_{gs2} explicitly shown and the associated equation describing the circuit is shown in [11]. The connection of the circuit dynamics with time scale separation model is shown in Table B.1

Two time scale model	Bistable circuit/charging-discharging capacitor combination model
$\frac{dx}{dt} = y$ $\epsilon\frac{dy}{dt} = -x + y - y^3$	$\frac{dV}{dt} = \frac{I_0}{C}z$ $g_m\epsilon\frac{dz}{dt} = 2(g_mR - 1)z - \frac{1}{4}z^3 - \frac{Vg_m}{I_0}$

Table B.1: Comparison of two time scale model and bistable circuit/charging-discharging capacitor combination model. The correspondence of two models is established

The two time-scale model exhibits two distinct phases: one during which energy is stored up slowly (slow time scale) and another in which the energy is discharged nearly instantaneously (fast time scale). During the slow time scale, $x \approx y - y^3$, $\frac{dy}{dt} \approx 0$. However, for all other points in the xy plane, $\frac{dy}{dt}$ tends to become large without limit as $\frac{1}{\epsilon} \to \infty$ and this is responsible for the fast time scale of the system.

On the left hand column of Table B.1 are the differential equations for the time scale separation model. On the right hand column of Table B.1 are the differential equations for the bistable circuit/charging-discharging capacitor combination model. Thus they have similar forms, which establish the connection.

It should be noted crudely speaking, in the bistable circuit/charging-discharging timing capacitor combination model, can identify the two time scale (slow-fast) dynamics as follows: timing capacitor C typically is much larger than parasitic capacitor. Thus, ϵ, associated with parasitic capacitor, tends to determine the fast dynamics, with C, the timing capacitor, determining the slow dynamics

The noise is dominated by regeneration/fast phase, as shown in [11]that the phase noise is peaked up during the regeneration; meanwhile phase noise during the charging/discharging is small, i.e. like $\frac{kT}{C}$.

Appendix C

Cryogenic Experiment Setup

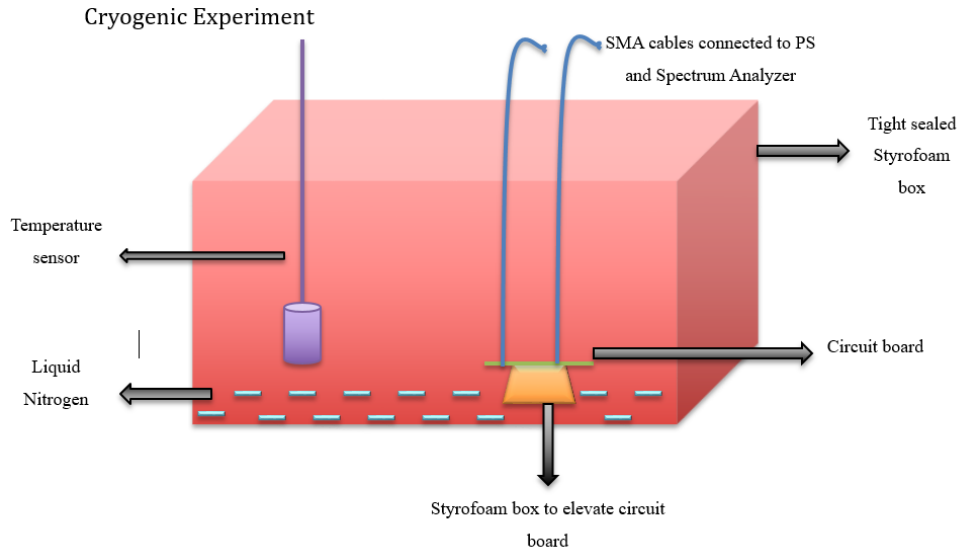

Figure C.1: Experiment Setup

Figure C.2: A photograph of the temperature sensor

Appendix D

The Regeneration Time Simulation of Relaxation Oscillator

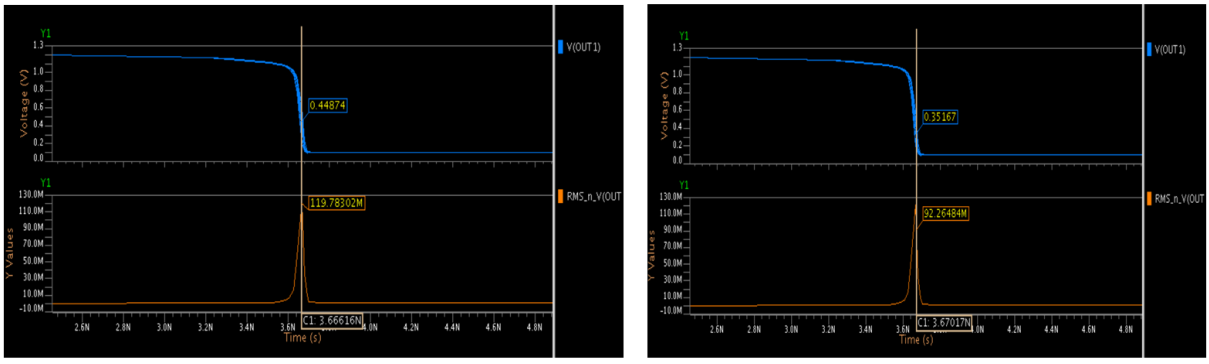

Figure D.1: The regeneration time of relaxation oscillator within 97mV overdrive voltage from the metastable voltage

The left graph of Figure D.1 shows that the voltage at metastable state is 0.44874V at time 3.66616ns. At this time, both the transistors are on. After approximately 0.4ps (as shown in the right graph of Figure D.1), the voltage drops by 97mV, and is approximately the overdrive voltage of the transistors. At this time, one of the transistor is turned off. So, the regeneration time is 4×10^{-13}s.

Appendix E

The Slew Rate Simulation of Relaxation Oscillator with Temperature Variation

Figure E.1 shows the change of slew rate in a function of temperature. The timing jitter is related to the noise amplitude such that $t_j = \frac{\mathcal{N}}{SR}$ with $\mathcal{N}$ is the noise amplitude, t_j is the time jitter and SR is the slew rate. The slew rate does not change much with temperature, thus the noise amplitude variation with temperature follows the same trend as jitter/phase noise variation. Specifically, the change in slope remains.

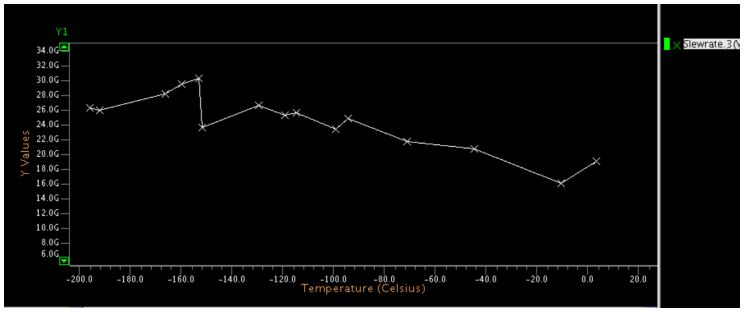

Figure E.1: The slew rate simulation of the relaxation oscillator with temperature drift. The temperature data points are obtained from the experiment temperature points of RO1

Appendix F

Background on Density Matrix as a Generalization of the Configuration Probability at Thermal Equilibrium to Include Quantum Mechanical Fluctuation

As with any microscopic description of many degree of freedom (internal degree of freedom) we start with the ensemble concept (see chapter 3). Remember classically to describe such ensemble, we use configuration/state and partition function to characterize it. In the generalization to quantum mechanics, the configuration state v becomes the quantum state, v, with the accompanying Boltzmann factor $e^{-\beta E_v}$ and partition function $\sum e^{\beta E_v}$. The quantum mechanical description uses the density matrix, whose diagonal element is just the Boltzmann factor (quantum), normalized by the partition function (quantum). In general, ensemble is a mixed ensemble with density operator given as

$$\rho = \sum_i w_i |\alpha^{(i)}\rangle\langle\alpha^{(i)}|. \tag{F.1}$$

and making a measurement on a mixed ensemble with observable, O, the ensemble average of can be denoted as

$$[O] = \sum_i w_i \langle\alpha^{(i)}|O|\alpha^{(i)}\rangle. \tag{F.2}$$

with $\langle\alpha^{(i)}|O_I|\alpha^{(i)}\rangle$ the quantum mechanical expectation value of O taken with respect to state $|\alpha^{(i)}\rangle$. Here, $|\alpha^{(i)}\rangle$ is the state ket of a pure ensemble i, and w_i is the fractional population of the pure ensemble i. The concept of probabilities manifests twice, with the first in $|\langle a'|\alpha^{(i)}\rangle|^2$ as the quantum mechanical probability for state $|\alpha^{(i)}\rangle$ to be found in O_I eigenstate $|a'\rangle$; and the second in w_i as the probability factor for finding in the ensemble of a quantum-mechanical state characterized by $|\alpha^i\rangle$.

As time evolves, with $t < t_{reg}$, w_i does not change much, but the quantum fluctuation from time evolution (or superposition can change: $e^{-\frac{Et}{\hbar}}$) manifests. The changes in $[O]$ is dictated by $e^{-\frac{Et}{\hbar}}$. After $t = t_{reg}$, w_i starts to change, and the change in $e^{-\frac{Et}{\hbar}}$ starts to cancel out, so the changes in $[O]$ is dictated by w_i. There is, however, not a whole lot of change, since by then w_i settle to $\rho_{kk} = \frac{\exp(-\beta E_k)}{\sum_l^N \exp(-\beta E_l)}$,where ρ_{kk} is the diagonal element of the density matrix. It stands for the fractional population for an energy eigenstate with energy eigenvalue E_k. The ensemble average of observable O_I can be written as

$$[O] \quad = \quad tr(\rho O). \tag{F.3}$$

Appendix G

Design Parameter of Fabricated Time-to-Digital Converter

Transistor: T14	$W_n/L_n(\frac{\mu m}{\mu m})$	7/0.12
Transistors: T13, T15, T16	$W_n/L_n(\frac{\mu m}{\mu m})$	3.5/0.12
Resistor: Oprrp0	$R(k\Omega)$	5
Transistors: T0, T1, T3, T5, T6	$W_n/L_n(\frac{\mu m}{\mu m})$	6.67/0.12
Transistors: T2, T4, T7	$W_n/L_n(\frac{\mu m}{\mu m})$	13.33/0.12
Capacitor: CM0	$C(fF)$	639.5
Comparators: I0, I3	-	-
SR-Flip flop: I4	-	-

Table G.1: Design Parameters of TDC as shown in Figure G.1

Transistor: T18	$W_n/L_n(\frac{\mu m}{\mu m})$	7/0.12
Transistors: T14,T15, T16, T17	$W_n/L_n(\frac{\mu m}{\mu m})$	14/0.12
Resistor: Oprrp12	$R(k\Omega)$	6
Transistors: T0, T1, T7, T6, T8, T9, T11, T10	$W_n/L_n(\frac{\mu m}{\mu m})$	1.4/0.12
Resistor: OPrrp0, Oprrp1, Oprrp7, OPrrp6, Oprrp8, Oprrp9	$R(k\Omega)$	8
Transistors: T2, T3, T12, T13	$W_n/L_n(\frac{\mu m}{\mu m})$	7/0.12

Table G.2: Design Parameters of Comparator shown in Figure G.2

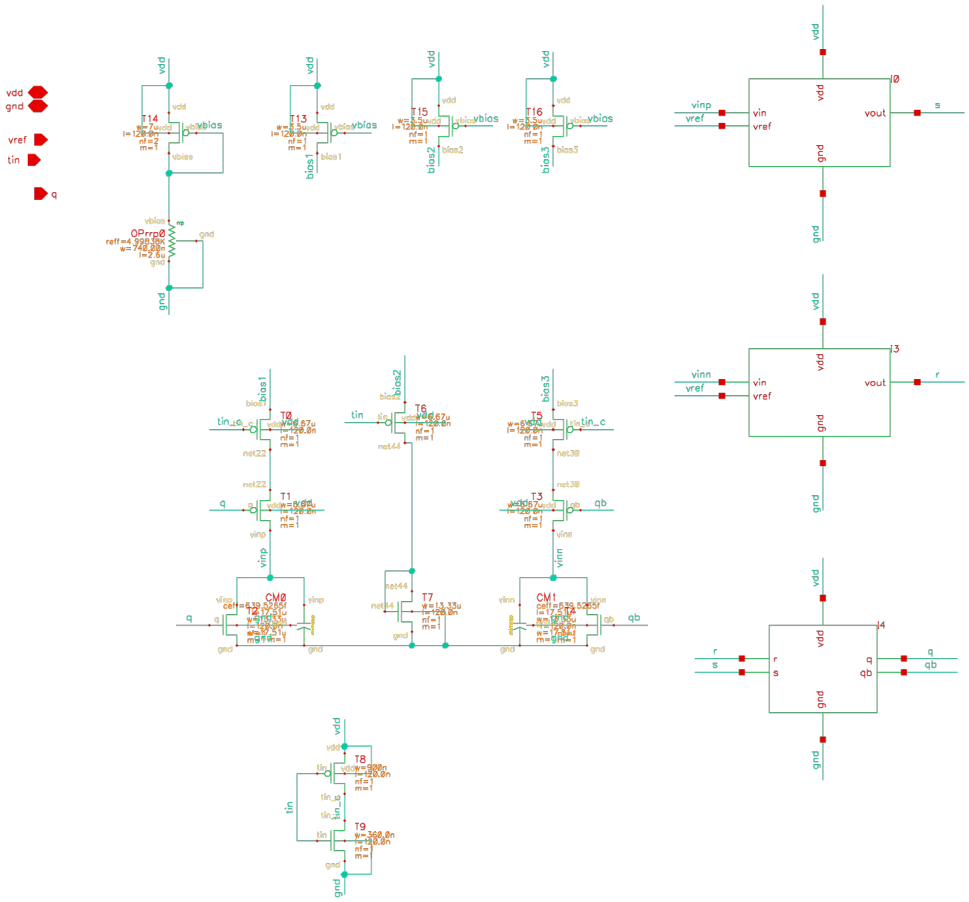

Figure G.1: The schematic of TDC

Transistors: T0, T1, T6, T7	$W_n/L_n(\frac{\mu m}{\mu m})$	2/0.12
Transistors: T2, T3, T4, T5	$W_n/L_n(\frac{\mu m}{\mu m})$	0.3/0.12

Table G.3: Design Parameters of SRFF as shown in Figure G.3

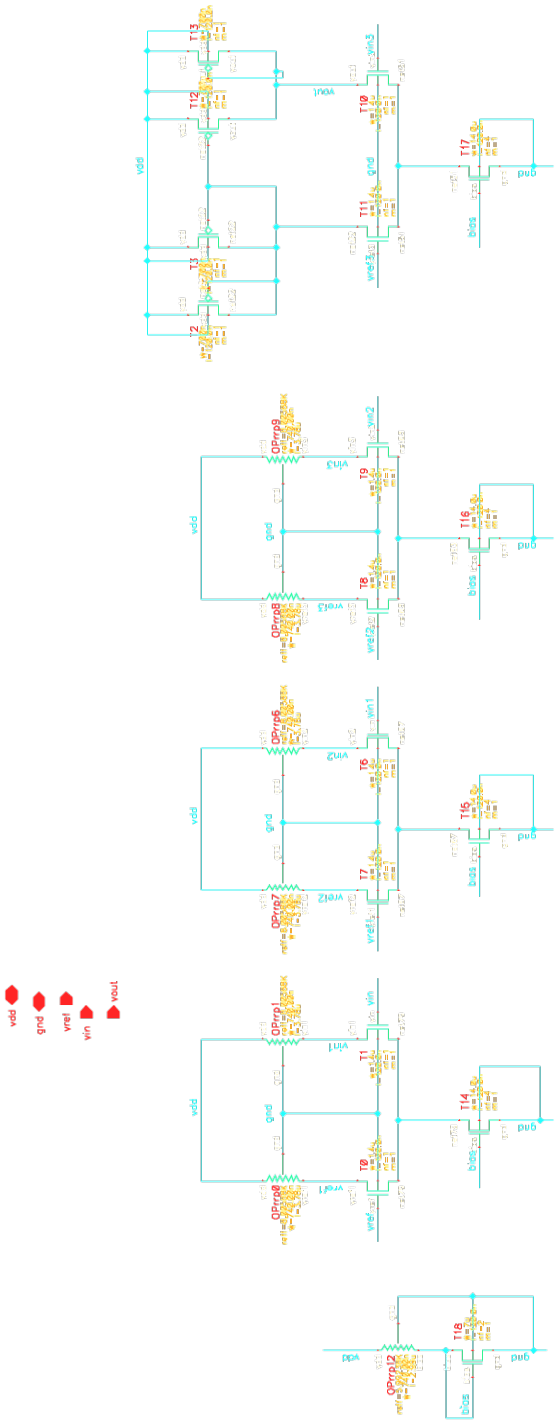

Figure G.2: The schematic of comparator

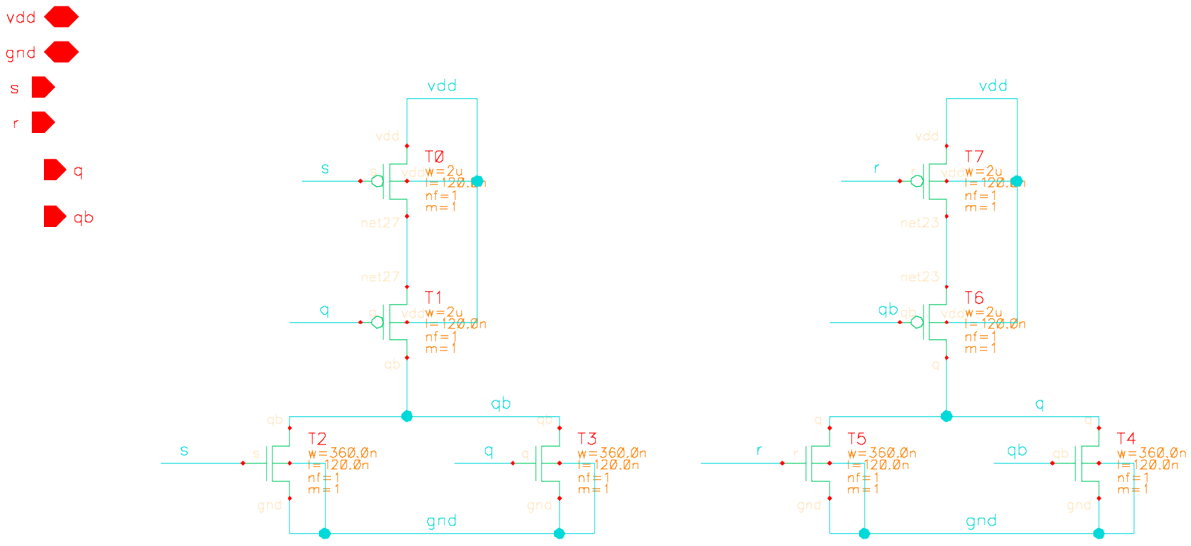

Figure G.3: The schematic of SR-flip flop